Cloud morphology and motions from Pioneer Venus images

Article *in* Journal of Geophysical Research Atmospheres · January 1981

DOI: 10.1029/JA085iA13p08107 · Source: NTRS

Anthony D Delgenio
NASA

JOURNAL OF GEOPHYSICAL RESEARCH, VOL. 85, NO. A13, PAGES 8107–8128, DECEMBER 30, 1980

Cloud Morphology and Motions From Pioneer Venus Images

WILLIAM B. ROSSOW, ANTHONY D. DEL GENIO, SANJAY S. LIMAYE,[1] AND LARRY D. TRAVIS

NASA Goddard Space Flight Center, Institute for Space Studies, New York, New York 10025

PETER H. STONE

Department of Meteorology, Massachusetts Institute of Technology, Cambridge, Massachusetts 02139

The orbiter cloud photopolarimeter on the Pioneer Venus spacecraft obtained over 300 images of Venus in the ultraviolet during a 3-month period of extensive observations from January through March 1979. The planetary scale and small-scale markings in the images provide information on the horizontal and vertical cloud structure, atmospheric waves, and wind speeds at the cloud top level. The images show evidence of long-term evolution of cloud properties and the atmospheric dynamics in addition to rapid small-scale changes in the cloud morphology. The polar regions are substantially brighter than at the time of Mariner 10 imaging. The planetary scale dark Y feature, previously identified in earth-based and Mariner 10 images, rotates about the planet with a period of 4–5 days but often changes dramatically from one appearance to the next and sometimes disappears entirely. Bow-shaped features and cellular features occur at all longitudes but are observed more easily near and downwind from the subsolar point. All of the cloud features exhibit a globally coordinated oscillation of their orientation relative to latitude circles. Retrograde zonal winds of ~ 100 m s^{-1} near the equator, similar to wind speeds observed from Mariner 10, are inferred from tracking of small-scale cloud features, but the two hemispheres exhibit significant differences. In the southern hemisphere the zonal wind speed decreases toward the poles at a rate similar to that for solid body rotation; the mid-latitude jet stream observed by Mariner 10 is not present. In the northern hemisphere, two jet streams are present with the mid-latitude jet stream weaker than that of the single northern hemisphere jet stream observed by Mariner 10. Meridional wind velocities are an order of magnitude weaker than the zonal velocities and are poleward in both hemispheres. The meridional wind speeds increase with increasing latitude up to mid-latitudes, with those in the northern hemisphere attaining higher values.

A. INTRODUCTION

The Pioneer Venus orbiter was placed in a high eccentricity, nearly polar, 24-hour orbit on December 4, 1978 [*Colin*, this issue]. The orbiter cloud photopolarimeter (OCPP) [*Russell et al.*, 1977; *Colin and Hunten*, 1977] began imaging and polarization mapping 1 day later. The objectives of this experiment are (1) to determine the physical properties, vertical and horizontal distribution, and temporal variability of the haze and cloud aerosols on Venus and (2) to record in near-ultraviolet images the variations in cloud morphology and the character of the cloud motions.

The OCPP design was optimized to use the long apoapsis portion of the orbit, during which the spacecraft longitude varies over only a small range. The most favorable illumination geometry for imaging thus occurs during approximately 100 days out of the 225-day Venus sidereal year. This periodic variation in illumination, together with the demands on the Deep Space Network for telemetry coverage, limits effective imaging to discrete periods (Figure 1). The first extensive imaging observations occurred during the nominal mission from December 1978 through March 1979 [*Travis et al.*, 1979*a*, *b*]. A second set of observations was obtained in the extended mission from October 1979 to November 1979, although the number of images was restricted by requirements for simultaneous Deep Space Network coverage of Pioneer Saturn and Voyager 2. A third imaging period was completed from March 1980 to June 1980. We report here on our progress in analyzing the imaging data obtained during just the nominal mission. *Kawabata et al.* [this issue] discuss the photopolarimetry results from the same period.

After a brief review in section *B* of previous UV imaging of Venus from earth and Mariner 10, we discuss in section *C* the properties of the images obtained by the OCPP. In section *D* we display a selection of the images and describe the characteristic cloud features and changes that they illustrate. Quantitative analysis of the brightness distribution in the images and of its temporal variation is presented in section *E*, while in section *F* we show the results of cloud-tracked wind studies. In section *G* we discuss these results and outline our current view of the implications for the dynamics and cloud structure of the upper atmosphere of Venus. We summarize our paper in section *H*.

B. PREVIOUS VENUS IMAGES

Venus is completely covered by clouds that are featureless in the visible but exhibit variable near-ultraviolet features long known to ground-based observers [*Wright*, 1927; *Ross*, 1928; *Boyer and Camichel*, 1961]. Subsequent ground-based images create a sporadic record of these features spanning more than 50 years, with more intensive coverage in 1962, 1967, and 1972 [*Dollfus*, 1975]. This data set provides valuable information about long time scale changes in the cloud features but is limited in two important aspects. First, the low spatial resolution of these images precludes examination of the smaller-scale details of the cloud changes. Second, the sporadic time coverage of these images makes precise determination of the time scales of variation difficult. Even during periods of more intensive observations the images are generally obtained on 1-day centers. (*Scott and Reese* [1972] and *Beebe*

---

[1] Presently at Space Science and Engineering Center, University of Wisconsin, Madison, Wisconsin 53706.

Paper number 80C0650.

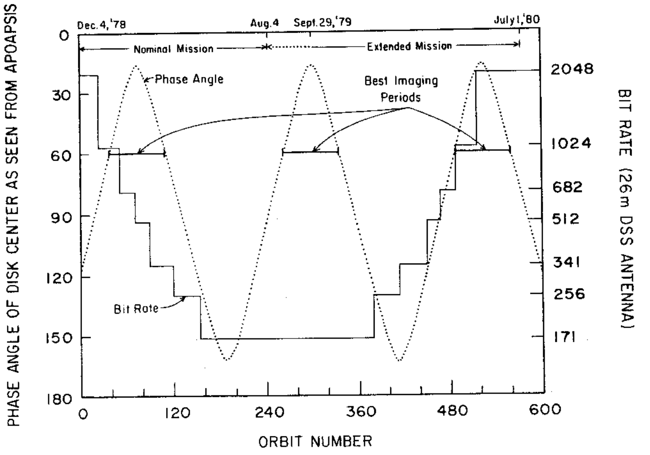

Fig. 1. The phase angle at the center of Venus as seen from the Pioneer Venus spacecraft at apoapsis through July 1980 (dotted line). A phase angle of 60° or smaller constitutes a 'good' imaging period, and these occur in winter 1979, fall 1979, and spring 1980. All of the images described in this paper are from the winter 1979 period. Also shown is the data transmission rate (bits per second) possible with the Deep Space Network 26-m antennas during the course of the mission (solid line); the transmission rate is higher for the 64-m antennas. In the fall of 1979 the 26-m bit rate was insufficient for imaging, and competition from Voyager and Pioneer Saturn precluded use of the 64-m antennas. The next good imaging period began in March 1980.

[1972] have shown that this can lead to spurious results when attempts are made to measure the apparent periodicity of the features' motions.) Nevertheless, several important properties of the largest-scale cloud features have been identified in this data set [*Dollfus*, 1975], as follows:

1. The global appearance of the Venus clouds varies on time scales ranging from ~1 day up to at least ~1 year.
2. On the shorter time scales of 1 day to 2 weeks, several recognizable features, viz., the dark horizontal 'Y' or 'Ψ' and the dark reversed 'C,' reappear quasi-periodically every 4 to 6 days before changing appearance after 1 or 2 weeks.
3. On the longer time scales of 1 month to 1 year the polar regions occasionally brighten relative to low and mid-latitudes.
4. The classical dark features are usually symmetric about the equator, but they can also exhibit significant asymmetry. Moreover, the two polar regions do not show any correlation between their brightness variations.

The Mariner 10 flyby of Venus in 1974 provided a complementary image data set to that obtained by ground-based observers [*Murray et al.*, 1974; *Belton et al.*, 1976*a*, *b*; *Anderson et al.*, 1978]. This image set contains valuable information on the small spatial and short temporal scales of variation of the cloud features which is currently unobtainable from earth. The high temporal and spatial resolution of the images in the first 3 days of the sequence allows the small-scale cloud features to be tracked to determine the wind velocities near the cloud tops [*Suomi*, 1974; *Limaye and Suomi*, 1980]. The primary limitation of this data set is the short time covered, which prevents a determination of the true time mean motions. In addition, care must be exercised in interpreting these images because the spatial resolution decreased by a factor ~10 and the temporal resolution decreased by a factor ~6 over the 8-day observing period. (*Belton et al.* [1976*a*] show that the former change produced some spurious interpretations when high-pass-filtered images were used.) Nevertheless, several important properties of the cloud features were inferred [*Murray et al.*, 1974; *Belton et al.*, 1976*a*, *b*], as follows:

1. Cloud features exhibit variations on all spatial scales down to ~30 km, but no isolated features of smaller scale are discernible.
2. Generally, the contrast and the variation time scale of the cloud features decreases with the size of the features.
3. In addition to the classical cloud features identified in ground-based images, several new types of cloud features exist in the Mariner 10 images which give important clues to the dynamics in this region. These features are discussed in section *D*.
4. If smaller-scale cloud feature motions reflect the true wind speeds, then the near 4-day periodicity of the larger-scale cloud features is consistent with the zonal wind at low latitudes but not with the regions of faster rotation in each hemisphere centered on 40° to 50° latitude. The larger-scale cloud features must therefore be propagating planetary scale waves. The meridional wind speed is small (typically ~5 m s^{-1}) and highly variable but poleward in both hemispheres on average.

C. PIONEER VENUS IMAGES

The OCPP images are produced by positioning the 3.7-cm Cassegrain telescope at a fixed angle (called the look angle) measured from the spacecraft spin axis; then the 5 rpm spin of the spacecraft scans the 0.4 × 0.45 mrad imaging field of view across the planet, while the motion of the spacecraft in its orbit translates the scan line across the planet for two-dimensional coverage [*Russell et al.*, 1977; *Travis et al.*, 1979*a*; *Travis*, 1979]. This spin-scan technique produces high-resolution (~30 km) images of the whole planet in about 4 hours with the high geometric fidelity required for quantitative analyses such as tracking of moving cloud features. The imaging mode uses a 365-nm filter with a single photodiode detector providing high photometric precision that allows for maximum feature enhancement. Further, the Pioneer Venus orbit produces images with nearly constant spatial resolution at all phase angles, independent of time scale, and gives a better view of the south polar region than attained previously. With the extended mission this data set will provide the link between the high spatial and temporal resolution observations of Mariner 10 and the low spatial and temporal resolution ground-based observations.

Since the intrinsic contrast of features in UV images of the Venus clouds is never larger than about 30% and, typically, 5–10% for smaller-scale features, the images must be enhanced in some fashion to aid detailed examination. The contrast of OCPP images is enhanced by high-pass filtering, with scales larger than about 30% of the disk diameter excluded. The images presented in this paper are a linear combination of these high-pass-filtered versions and the original data, all weighted in the same manner to reveal both the small- and large-scale features. Simple 'normalization' of the images to remove the large-scale variation in intensity caused by solar zenith angle variation over the disk does not reveal the small-scale features as well as filtering because their relative contrast is much smaller than that between the polar and equatorial regions (cf. Figure 2*a* in this paper and Figure 3 of *Travis et al.* [1979*a*]). This image processing, together with variations in the developing and printing of images, can change the relative prominence of features. Therefore we have been careful to use the raw data to verify all features discussed in this paper (cf. discussion following Figure 2 of *Travis et al.* [1979*a*]). The high photometric quality of the OCPP images is demonstrated by the many readily identified small-scale (~100 km) features in the images (e.g., Figure 8) and by the repetition of low-contrast features in adjacent scan lines of digital data.

A primary obstacle to the interpretation of cloud variations and motions in OCPP images in terms of atmospheric dynamics is that we do not know what produces the UV features. This uncertainty means that we do not know what changes in atmospheric properties accompany the observed changes in the cloud features. Without this information an observer looks for foreground and background objects in the images as one of many techniques to structure and interpret a changing visual scene. Consequently, these images create a Rorschach test in which we run the dangers of having our attention focused on a bright or dark area because its shape is vaguely familiar and of imposing a foreground-background interpretation where none may exist. Furthermore, temporary juxtapositions of features may produce the impression that several unrelated pieces are actually part of a coherent cloud structure. These effects mean that conclusions about the feature relationships and variations will depend on the spatial and temporal coverage of the image data set. Since the OCPP images cover a much longer time period than Mariner 10 images and have higher spatial resolution than ground-based images, our impressions of the cloud variations will differ from those of other workers. Eventually, the analysis of correlations in cloud and atmospheric behavior, revealed in other OCPP measurements [*Travis et al.*, 1979*a*] and data from other instruments on Pioneer Venus [*Colin*, this issue], should improve our interpretations of the UV images.

D. DESCRIPTION OF THE ALBEDO PATTERNS

In this section we describe the time variation of the appearance of Venus in images spanning roughly a month and a half centered on the time of zero phase angle. (The phase angle is the angle between the sun-Venus and the spacecraft-Venus directions. Since phase angles for different locations on the visible disk vary at most by ~15°, we adopt the value at the disk center as characteristic of the whole image.) These images are shown in Figures 2 and 3 with the north pole at the top, the morning terminator on the right in Figures 2*a*–2*o*, and the evening terminator on the left in the remaining images. The retrograde rotation of the planet and the cloud features appears as motion to the left. The dates of acquisition and the time, phase angle, and latitude of the image center are listed in Table 1 for all the images studied in this paper.

Each image in Figures 2 and 3 can be divided into three different latitude regimes: a polar regime poleward of about 45°–50° latitude in each hemisphere, a mid-latitude regime between 20° and 45°–50° latitude in each hemisphere, and an equatorial regime between ±20° latitude. Each is characterized by its particular mean brightness and set of smaller-scale features that give that region a particular 'texture.' In most cases, we adopt the convention of describing these smaller features as 'dark objects on a bright background.' This distribution of region types, along with the feature nomenclature used in this paper, is illustrated in Figure 4. These drawings represent two characteristic appearances of Venus, about 2 days apart, and should aid the reader in locating specific features in Figures 2 and 3. Examples of all the features labeled in Figure 4 are discussed below.

1. Polar Regions

The polar regions in Figures 2 and 3 appear brighter than the rest of the planet even though the scattering geometry would cause the poles of an isotropically scattering sphere to appear much darker than the equatorial region. This is also shown by the latitudinal variation of the maximum raw intensity (Figure 5). The prominent bright south polar band in the Mariner 10 images, on the other hand, is not the brightest part of the planet in the raw data, and the greater intrinsic brightness of the whole south polar region is not evident until the scattering geometry effects are removed [*Limaye and Suomi*, 1977]. From this comparison of the raw image brightness distributions we conclude that the first period of Pioneer Venus observations corresponds to a time of polar brightening as defined by ground-based observers, while the Mariner 10 epoch does not [see *Kawabata et al.*, this issue].

The polar regions generally exhibit a two-part structure. The brightest part, between 45° and 65° latitude, is labeled the bright polar band in Figure 4. A slightly darker polar cap exists at higher latitudes. About 50% of the time, one or more narrow dark polar bands separate the bright polar band from the polar cap (e.g., Figures 2*c* and 2*t*). The general absence of smaller-scale features in the polar regions gives them a typically 'smooth' appearance.

In most of the images the two polar regions are similar in shape and extent. The smaller apparent size of the north polar region is caused by the southerly latitude of the subspacecraft point in most of the images (Table 1). (Figures 2*e* and 2*f* illustrate the effect of changing viewing position on the apparent size of the polar regions.) However, near the end of the first imaging period the boundary of the north polar region moved equatorward with a substantial increase in the size of the north bright polar band (Figures 3*b* and 3*c*). The most important variation in the polar regions is the quasi-periodic change of the alignment of all the polar bands from tilted (Figures 4*a* and 2*l*) to zonal (Figures 4*b* and 2*r*). Both polar regions undergo this variation in a coordinated fashion, while the smaller-scale features seem less coordinated, as illustrated by Figures 2*f* and 2*x*.

Figure 6 shows details of three characteristic types of small-scale structure which appear on the equatorward edge of the polar regions. Figure 6*a* shows the whorl-like or ragged structure of the bright south polar band described by the Mariner 10 imaging team [*Murray et al.*, 1974]. The bright streamers (Figures 4*b*, 2*j*, and 2*r*) often form a fan-shaped set that suggests the presence of bright material in quite low latitudes. On the other hand, Figure 6*b* suggests the presence of darker 'mid-latitude' material in the polar region (cf. Figures 2*o* and 2*w*). This unusual structure formed the leading edge of the indistinct polar boundary in Figure 2*e*. These two types of features suggest a dynamic interaction between the polar and mid-latitude regions. Occasionally, the ragged boundary is replaced by a sharp, curvilinear boundary (Figure 6*c*). The contrast between the bright polar band and the dark mid-latitude band (section D2) in this image is one of the highest in the whole image set. The darker material on the right end of the bright polar band is the leading edge of a new whorl-streamer pattern (Figure 2*m*) which is much less prominent than the one in Figure 6*a*.

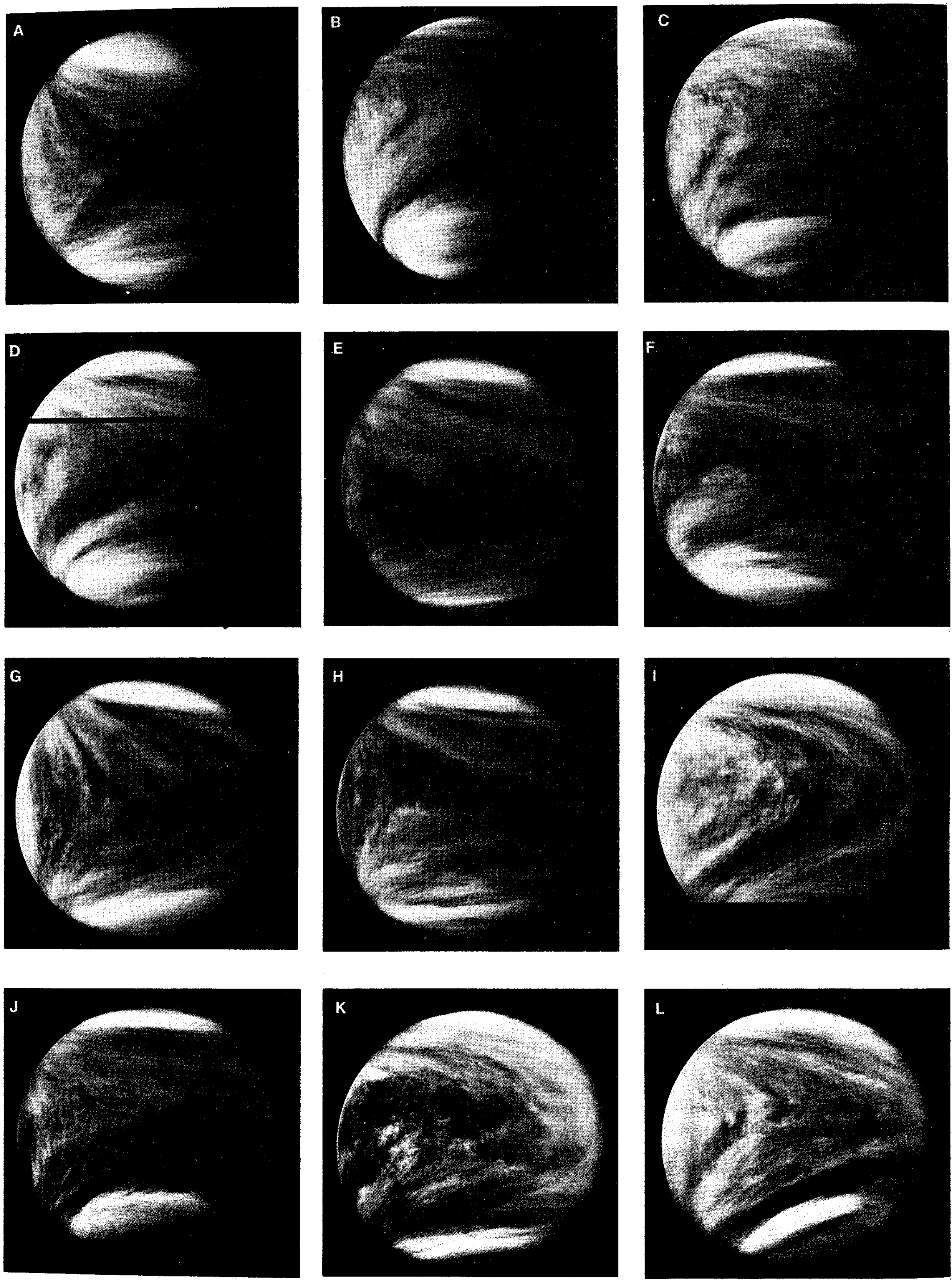

Fig. 2. Pioneer Venus OCPP images.

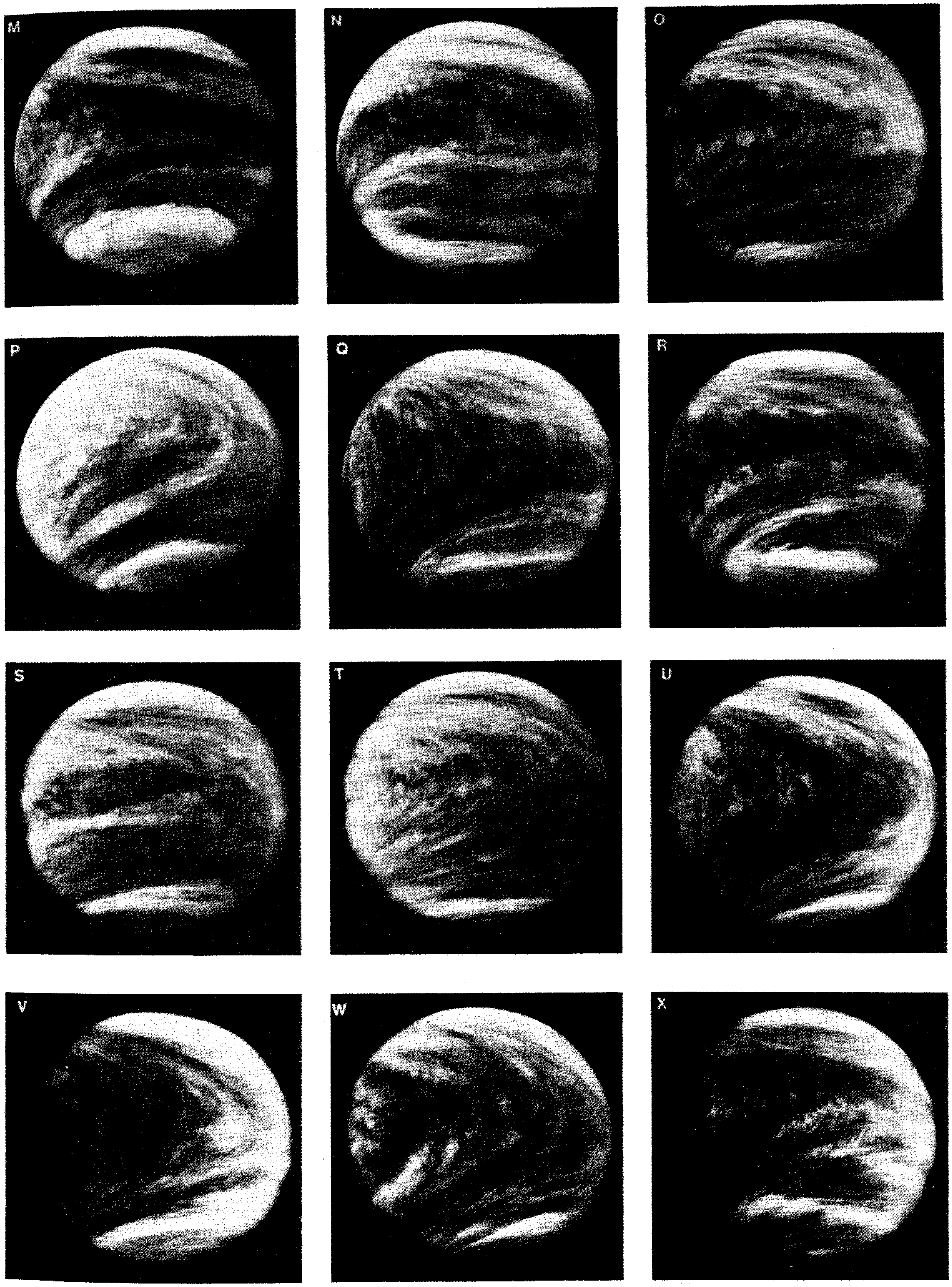

Fig. 2. continued

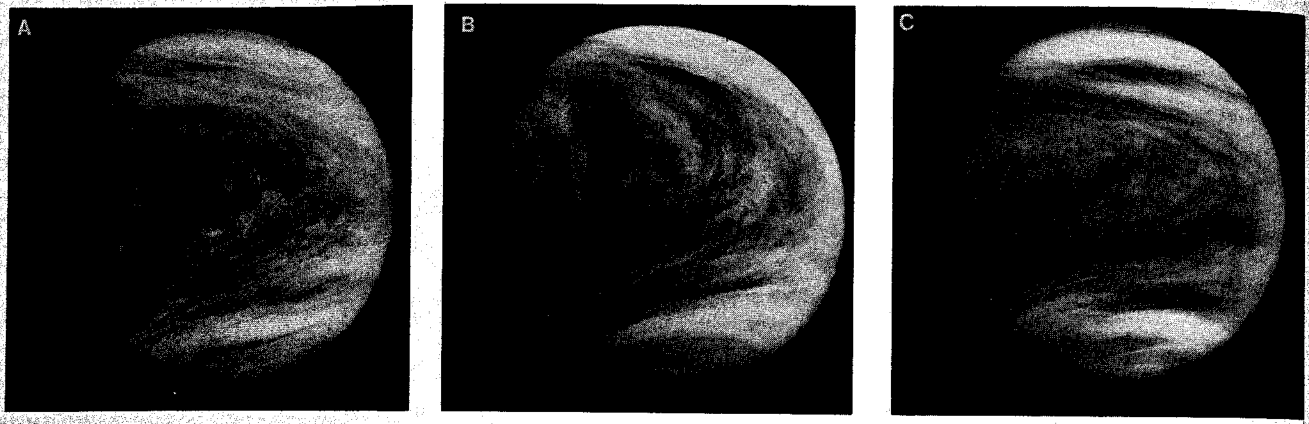

Fig. 3. Pioneer Venus OCPP images.

These complex spatial structures vary rapidly in time, making interpretation of the images difficult. The changing appearance of the polar regions cannot, for example, be simply explained by a single longitudinal pattern advected around the planet. In most cases the advection of a polar feature can be observed in images separated by less than a day, but the same feature cannot be recognized 4 or 5 days later. Consider, e.g., the 5-day sequence, Figures 2*l*–2*q*. In going from Figure 2*l* to 2*m* the lower contrast portion of the southern bright polar band has moved from the right edge to the left and is clearly recognizable in the images between these two (e.g., Figure 6*c*). Even this very striking configuration is completely altered 4 and 5 days later (Figures 2*p* and 2*q*, respectively). Other more rapidly changing features are also apparent in the original images but are difficult to discern in Figures 2 and 3.

2. *Equatorial and Mid-Latitude Regions*

The images in Figures 2 and 3 exhibit a large variety of dark shapes in middle and low latitudes. Since the larger-scale markings typically extend over all latitudes between 50°N and 50°S, we consider these two regions together. These shapes can be assembled, in most cases, from three basic features (Figure 4): (1) bow-shaped features (Figure 3*a* and *Travis et al.* [1979*b*]), (2) dark mid-latitude bands (Figure 2*l*), and (3) a dark equatorial band (Figure 2*r*). Every image in Figures 2 and 3 contains one or more of these three features.

a. Bow-shaped features. When continuous, planetary scale, bow-shaped features such as those in Figures 3*a* and 4*a* are not evident (about 50% of the time), the smaller streak features of the mid-latitude regions, which are present in most of the images, still impart a V shape to the cloud patterns (cf. Figure 2*j*). Even in images where the large-scale features are more zonal in appearance (Figure 2*n*), the mid-latitudes still exhibit the smaller streak features. These streak features are the most ubiquitous feature we have observed in the Venus clouds. The large bow-shaped features are the 'bowlike waves' and the small streak features are the so-called 'spiral streaks' first identified by the Mariner 10 imaging team [*Murray et al.*, 1974]. Our impression from observing the variation of these features over 100 days is that they are really different manifestations of the same phenomenon. This impression is supported by the occasional appearance of features intermediate in scale and coherence between the two extremes of many thin, short, aligned features and a few thick, planetary scale features (Figure 2*t*). Even well-defined bow-shaped features, as in Figure 3*b*, often break down into a series of smaller-scale features when viewed in enlargement (Figure 7). Consequently, we propose that all such markings be grouped under the label 'bow-shaped features' in order to emphasize the tilted alignment common to most of the cloud patterns. Thus in Figure 4*b* we label the smaller mid-latitude streaks as bow shapes. However, we continue to refer to two varieties of bow-shaped features (large and small) when describing aspects of the morphology which are scale dependent.

Figure 2*t* illustrates the nearly uniform longitudinal distribution typical of the small bow-shaped features. Large bow-shaped features also occur in both the morning (Figure 2*c*) and evening (Figure 3*a*) quadrant, contrary to the impression obtained from the Mariner 10 images [*Murray et al.*, 1974]. Nevertheless, these features are clearly more obvious in the evening quadrant. This longitudinal asymmetry is responsible for the characteristic 'reversed C' appearance of Venus in ground-based evening terminator images (cf. Figure 3). When the bow shapes are prominent in mid-latitudes, they generally do not extend past the equatorward edge of the bright polar region, but they frequently compose the dark part of the 'ragged boundary' structure (Figure 2*r*) discussed in section *D1*. Occasionally, however, one (Figure 2*o*) or more (Figure 2*w*) of the large bow shapes do cross the boundary of the bright polar region and extend well into the polar cap region. At times these crossing dark streaks appear to break the bright polar band completely (Figure 2*p*). Similar behavior is apparent for the northern hemisphere, although our view is poorer.

The bow-shaped features are tilted ~30°–45° with respect to latitude circles at mid-latitudes. At low latitudes their tilt varies with time from 90° (Figures 4*a* and 2*t*) to nearly zero (Figures 4*b* and 2*r*). This variation is coordinated with that of the polar bands (section *D1*) and determines the vertex angle of the 'V' shape which dominates the images. Generally, when both large and small bow-shaped features are present, they have the same tilt angles at all latitudes. However, there are examples where the large bow shapes exhibit more than one tilt angle (Figure 2*g*) or cut across the small bow shapes (Figure 2*w*).

b. Dark mid-latitude bands. The dark mid-latitude bands (Figure 4*a*) seem to be thicker bow-shaped features. Occasionally, they appear as distinct, high-contrast features (cf. Figures 2*b* and 2*l*), but generally they are less prominent. During some periods these features join at the broad end of the dark equatorial band to form the classical dark horizontal Y feature

TABLE 1. Image Information

		Image Center			
Image Number	Date	Universal Time	Phase Angle	Latitude	Use*
26	Dec. 17, 1978	0226	99°	22°S	Fig. 9
35	Dec. 22, 1978	1257	84°	7°N	T
36	Dec. 23, 1978	1200	84°	2°N	T
37	Dec. 24, 1978	1209	82°	2°N	T
40	Dec. 25, 1978	1220	80°	2°N	T
41	Dec. 26, 1978	1229	79°	2°N	T
42	Dec. 27, 1978	1317	76°	5°N	T
43	Dec. 28, 1978	1235	76°	1°N	T
44	Dec. 29, 1978	1327	73°	4°N	T
45	Dec. 30, 1978	1335	72°	4°N	T
46	Dec. 31, 1978	1303	71°	1°N	T
47	Jan. 1, 1979	1319	69°	2°N	T
48	Jan. 2, 1979	1319	67°	2°N	T
49	Jan. 3, 1979	1332	66°	3°N	T
53	Jan. 4, 1979	1315	64°	0°	T
57	Jan. 5, 1979	1316	63°	0°	T
61	Jan. 6, 1979	1326	61°	0°	T
65	Jan. 7, 1979	1332	60°	0°	T
69	Jan. 8, 1979	1337	58°	0°	T
73	Jan. 9, 1979	1342	56°	0°	T
78	Jan. 10, 1979	1347	55°	0°	Fig. 2*a*, T
83	Jan. 11, 1979	1357	53°	1°N	T
88	Jan. 12, 1979	1401	51°	1°N	T
93	Jan. 13, 1979	1406	50°	1°N	T
94	Jan. 14, 1979	0546	56°	22°S	Fig. 2*b*
98	Jan. 18, 1979	0602	51°	22°S	Fig. 2*c*, Fig. 10
102	Jan. 19, 1979	0958	44°	13°S	Fig. 2*d*
117	Jan. 23, 1979	0540	44°	23°S	Fig. 6*b*
118	Jan. 23, 1979	1504	33°	2°N	Fig. 2*e*
122	Jan. 24, 1979	1510	32°	2°N	M, S
126	Jan. 25, 1979	1514	30°	2°N	M, S
130	Jan. 26, 1979	1515	28°	3°N	M, S
133	Jan. 27, 1979	1243	29°	7°S	Fig. 2*f*, M, S
138	Jan. 28, 1979	1248	27°	6°S	M, S
144	Jan. 29, 1979	1250	26°	6°S	M, S
150	Jan. 30, 1979	1249	24°	7°S	Fig. 2*g*, M, S
156	Jan. 31, 1979	1253	22°	7°S	Fig. 2*h*, M, S
162	Feb. 1, 1979	1258	21°	6°S	M, S
168	Feb. 2, 1979	1229	20°	8°S	M, S
170	Feb. 3, 1979	0930	23°	15°S	Fig. 2*i*
174	Feb. 5, 1979	0932	22°	15°S	Fig. 2*j*
175	Feb. 5, 1979	1426	13°	2°S	M, S
181	Feb. 8, 1979	0420	29°	27°S	W
182	Feb. 8, 1979	0927	17°	15°S	Fig. 2*k*, Fig. 8, W
183	Feb. 8, 1979	1424	8°	2°S	M, S, W
185	Feb. 9, 1979	0420	28°	27°S	W
186	Feb. 9, 1979	0926	16°	15°S	W
187	Feb. 9, 1979	1423	6°	2°S	M, S, W
189	Feb. 10, 1979	0419	28°	27°S	W
190	Feb. 10, 1979	0927	15°	15°S	Fig. 2*l*, W
191	Feb. 10, 1979	1422	5°	2°S	Fig. 6*c*, M, S, W
193	Feb. 11, 1979	0346	29°	29°S	W
194	Feb. 11, 1979	0844	16°	17°S	Fig. 2*m*, W
195	Feb. 12, 1979	0345	28°	29°S	W
196	Feb. 12, 1979	0843	15°	17°S	Fig. 2*n*, W
197	Feb. 13, 1979	0343	28°	29°S	W
198	Feb. 13, 1979	0840	15°	17°S	Fig. 2*o*, W
199	Feb. 14, 1979	0342	27°	29°S	Fig. 2*p*
201	Feb. 15, 1979	0344	27°	29°S	W
202	Feb. 15, 1979	0830	15°	17°S	Fig. 2*q*, W
203	Feb. 16, 1979	0404	25°	28°S	W
204	Feb. 16, 1979	0908	13°	16°S	Fig. 2*r*, Fig. 6*a*, W
205	Feb. 16, 1979	1409	5°	2°S	M, S, W
207	Feb. 17, 1979	0422	24°	27°S	W
208	Feb. 17, 1979	0928	13°	15°S	Fig. 2*s*, W
209	Feb. 17, 1979	1424	7°	1°S	M, S, W
211	Feb. 18, 1979	0419	24°	27°S	W
212	Feb. 18, 1979	0927	13°	15°S	Fig. 2*t*, W
213	Feb. 18, 1979	1421	8°	1°S	M, S, W
215	Feb. 19, 1979	0416	25°	27°S	W

TABLE 1. (continued)

Image Number	Date	Image Center Universal Time	 Phase Angle	 Latitude	Use*
216	Feb. 19, 1979	0921	14°	14°S	Fig. 2*u*, W
217	Feb. 19, 1979	1417	10°	2°S	M, S, W
219	Feb. 20, 1979	0412	25°	27°S	W
220	Feb. 20, 1979	0919	14°	15°S	Fig. 2*v*, W
221	Feb. 20, 1979	1416	11°	2°S	M, S, W
225	Feb. 21, 1979	1406	13°	2°S	M, S
232	Feb. 24, 1979	0816	20°	17°S	Fig. 2*w*
237	Feb. 26, 1979	0805	22°	17°S	Fig. 2*x*, Fig. 11
248	March 1, 1979	0558	27°	22°S	W
249	March 1, 1979	1103	25°	10°S	M, S, W
257	March 2, 1979	1057	26°	10°S	M, S
264	March 3, 1979	0614	29°	21°S	W
265	March 3, 1979	1118	28°	9°S	Fig. 3*a*, M, S, W
272	March 4, 1979	0610	31°	21°S	W
273	March 4, 1979	1113	29°	9°S	M, S, W
278	March 5, 1979	0603	32°	21°S	W
279	March 5, 1979	1107	31°	9°S	M, S, W
284	March 6, 1979	0557	33°	21°S	W
285	March 6, 1979	1101	32°	9°S	M, S, W
290	March 7, 1979	0551	35°	21°S	Fig. 3*b*, W
291	March 7, 1979	1054	34°	9°S	Fig. 7, M, S, W
296	March 8, 1979	0545	36°	21°S	W
297	March 8, 1979	1048	35°	9°S	W
303	March 9, 1979	1040	37°	9°S	Fig. 3*c*
308	March 12, 1979	1021	41°	10°S	W
309	March 12, 1979	1447	46°	5°N	W
321	March 24, 1979	1040	60°	11°S	W
322	March 24, 1979	1451	63°	2°N	W
323	March 26, 1979	1055	63°	10°S	W
324	March 26, 1979	1515	67°	3°N	W

*Denotes the types of analyses for which each image is used. Images reproduced in this paper are designated by the appropriate figure number. Images used in quantitative analyses are indicated by one of the following: M, moments of brightness distribution; S, power spectra; T, time series; and W, cloud-tracked winds.

(e.g., Figures 2*p*–2*q* and 2*t*–2*u*). At other times, they coexist with and nearly parallel the dark equatorial band (cf. Figures 2*d*, 2*f*, 2*k*, and 2*m*). Often the dark mid-latitude bands appear as a pair of dark bands separated by a thinner bright band (Figures 2*m* and 2*p*) called a 'spiral band' in the Mariner 10 images [*Belton et al.*, 1976*b*]. In extreme cases (Figures 2*q* and 2*u*) the 'arms' of the Y feature, which we have identified as dark mid-latitude bands, seem to be composed of several large bow-shaped features. In Figure 2*g* the dark bands coexist with several additional large bow shapes to the left, while in Figure 2*i* there seem to be two sets of dark arms. These images suggest that the dark mid-latitude bands and the arms of the Y feature are actually larger, higher-contrast examples of large bow-shaped features.

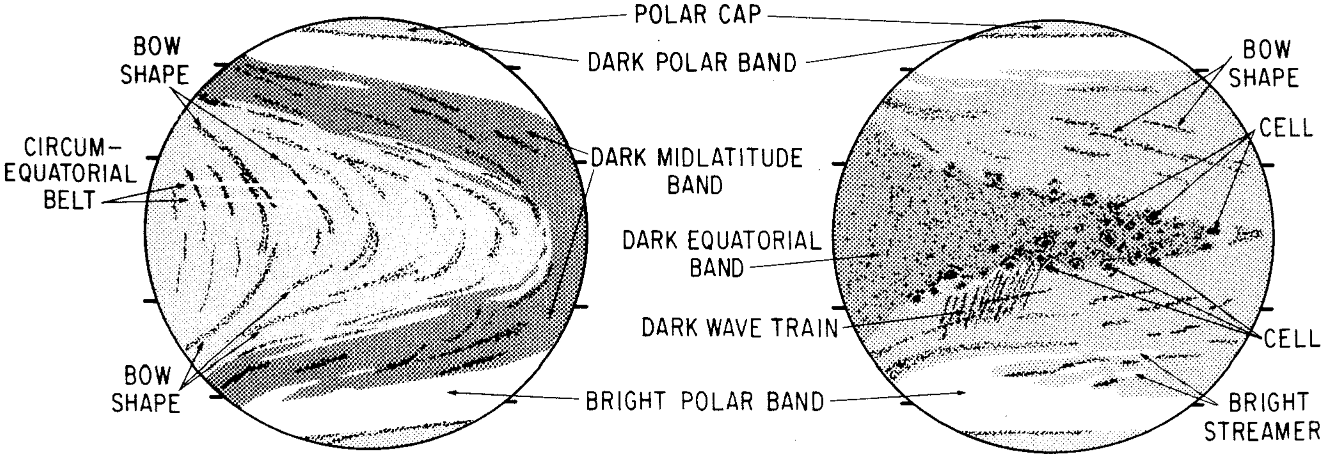

Fig. 4. Schematic diagram defining the basic types of cloud features observed in Venus ultraviolet images. The two views depicted here typically occur 2 days apart and represent the maximum and minimum tilt configurations, respectively. The tick marks on each circle indicate 20° and 50° of latitude in each hemisphere.

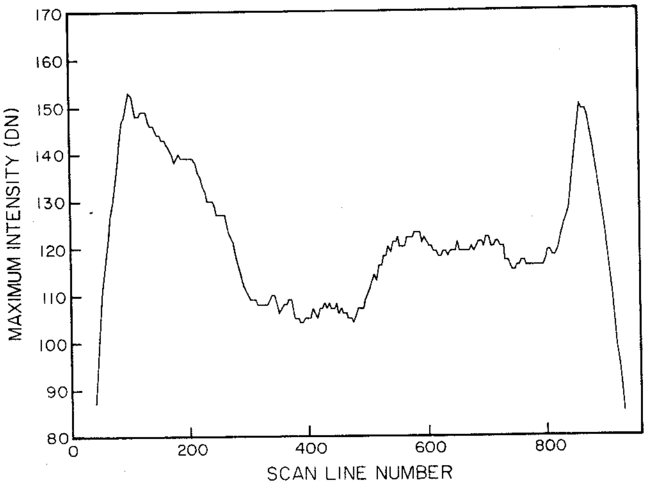

Fig. 5. The raw maximum intensity of each scan line as a function of the scan line number across the disk of Venus for a typical image. The scan line number roughly corresponds to a specific latitude on Venus in this image.

c. Dark equatorial band. Examples of the dark equatorial band are shown in Figures 2*r* and 2*u*. In the latter image the dark band forms the 'tail' of the Y feature. The presence of the dark equatorial band is always associated with a nearly zonal alignment of the other features, giving the images a zonally symmetric appearance (Figure 4*b*). This appearance characterizes slightly less than half of the images. Generally, the dark equatorial band lies symmetrically along the equator, but about one third of the time, it shifts toward one hemisphere (Figure 2*x*) or exhibits a more irregular shape (Figures 2*f* and 2*h*). The dark band is always latitudinally broader at the downstream (left) end than the mean width (~40°). This end of the dark band is usually associated with the large bow-shaped features, dark mid-latitude bands, or both, producing a Y feature. The upstream end is always narrower than the mean, often coming to a point (Figure 2*s*). The length of the dark band is variable, covering anywhere from ~120° to ~270° of longitude. (These lengths can be deduced from two image sequences, Figures 2*u*, 2*v*, and Figures 2*q*, 2*r*, and 2*s*, respectively, by assuming that the features move at roughly 100 m s^{-1} or 90°/d.)

Low and mid-latitudes are characterized by their mottled appearance. This appearance is the consequence of several small-scale features called cells, circumequatorial belts, and dark wave trains (Figure 4).

d. Cells. The Mariner 10 imaging team recognized another common small-scale feature, besides the 'streaks,' namely, the cellular features [*Murray et al.*, 1974]. The majority of the OCPP images also show these cells. The enlargement in Figure 8 illustrates the generally scattered, irregular pattern formed by the cells. This pattern seems composed of both larger (~500–1000 km in diameter) diffuse bright cells with dark rims and smaller (~200–500 km) dark cells with bright rims. An especially prominent example of the latter variety is shown in Figure 9.

Murray et al. [1974] and *Belton et al.* [1976*b*] concluded that the cells occur preferentially in the equatorial region near and downstream of the subsolar region forming a 'subsolar disturbance' which is 'continually being regenerated there.' OCPP images confirm this distribution in low latitudes between ±20° and at longitudes near and downstream of the subsolar point. In addition, cells seem more prevalent when the equator is dark than when it is bright. This distribution is associated with the generally higher contrast in images with a dark equator (Figure 2*k*) when compared to images with a bright equator (Figure 2*t*) or in images of the evening terminator (Figure 3*c*) when compared to images of the morning terminator (Figure 2*d*). However, cells do occur at higher latitudes (Figure 9), near the morning terminator (Figures 2*b* and 2*n*) and in bright equatorial regions (Figure 2*t*), so the distribution of cells may reflect improved visibility associated with darker regions rather than the intrinsic distribution of the cells (see section *G2*).

We confirm the conclusions of *Murray et al.* [1974] and *Belton et al.* [1976*b*] regarding the lifetimes of the cells. Larger cells persist from one image to another taken about 5 hours later, and occasionally to a third 10 hours later, indicating a lifetime of the larger cells between 6 and 24 hours. However, the smaller cells do not persist in images taken more than 3 hours apart.

e. Wavelike features. The Mariner 10 images, covering 8 days, showed a train of wavelike features, about 5000 km long with a separation of ~500 km, propagating southward near the equator [*Murray et al.*, 1974; *Belton et al.*, 1976*b*]. We have seen these 'circumequatorial belts' (Figures 2*c*, 2*p*, and 10) several times in our 3 months of imaging. In addition, we have identified several occurrences of a new type of wave phenomenon which takes the form of short (~2000 km), dark streaks separated by ~200 km and lying at a large angle to the equator (Figure 11). (A similar but much smaller feature was noticed in a few Mariner 10 images by *Belton et al.* [1976*b*].) Like the circumequatorial belts, these features cut across the background trend of low and mid-latitude bow shapes (cf. Figure 4).

3. *Short History of the Y Feature*

In this section we focus on the relationships between the principal albedo features described above by examining the changing appearance of the classical Y feature. The Y feature appears to be a composite structure formed by the correlated appearance of two or possibly three separate features. The variations in the separate features lead to large changes in the appearance of the Y feature and, at times, to its disappearance. These correlations do not occur entirely by chance, but rather they are reasonably coherent and quasi-periodic events. In particular, the evolution of the tilt of all the cloud features with respect to latitude circles seems to follow a regular sequence, oscillating between the extreme configurations illustrated in Figure 4 with an approximate 4-day period. To emphasize this regular sequence as well as variations away from it, we arrange the images in Figures 2 and 3 into 4-day cycles in Table 2. (The blanks in this table represent images which exist but are not shown here.)

In the early images the disk is not fully illuminated, so a complete Y feature can only be inferred from a time sequence. Figures 2*a* and 2*b*, separated by 4 days, show the recurrence of the well-defined Y feature observed for at least six cycles during this early period. In the next cycle, however, the arms of the Y feature are no longer evident (Figure 2*c*), but many bow-shaped features have appeared. The next day (Figure 2*d*) the pattern takes the shape of a dark wedge which resembles a Y shape, but with the tail and the northern hemisphere arm less prominent. If the bright feature at the equator on the left

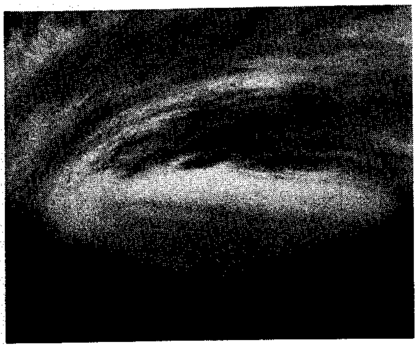

Fig. 6*a*

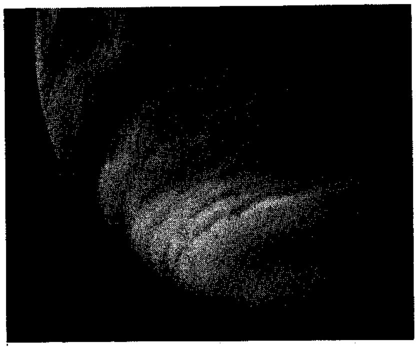

Fig. 6*b*

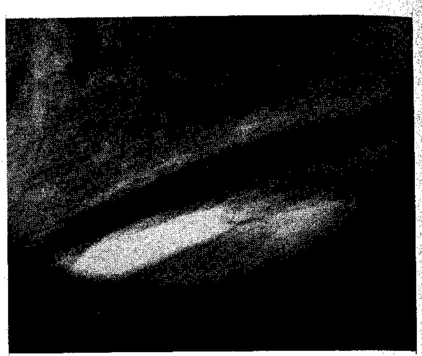

Fig. 6*c*

Fig. 6. Characteristic features seen in the south polar region in OCPP images. (*a*) Bright streamers extend from the bright polar band to lower latitudes, creating a whorl-like structure in this blowup of Figure 2*r*. (*b*) At least three unusually narrow dark bands are apparent near the limb in the south polar region. (Image acquired ~9 hours before Figure 2*e*.) (*c*) An unusually dark region parallels the relatively smooth edge of an unusually bright polar band, which is disrupted by dark material to the right. (Image acquired ~5 hours after Figure 2*l*.)

marks the 'vertex' of the Y feature, then a phase shift of about 45° has apparently occurred. In the next three cycles (Figures 2*e*–2*h*) the pattern becomes highly asymmetric and distorted with no clearly recognizable Y feature present. Near the end of this period, many large bow shapes appear (Figure 2*g*), presaging the appearance of the striking feature in Figure 2*i*. This new feature undergoes several modifications over the next two cycles, culminating in an irregular Y feature similar to that observed by Mariner 10 (cf. Figure 2*m* and images of *Murray et al.* [1974]). Table 2 shows that this new Y feature is in phase with the Y feature in cycle two. The image sequence, Figures 2*l*–2*u*, covers 10 days during which the Y feature undergoes dramatic modification during each 'rotation' but remains recognizable. Of particular note is the change in the length of the dark equatorial band during this time (see discussion in section *D2c*).

At the end of this three cycle period (9–11), the phase of the Y feature again appears to undergo a large shift before disappearing. In Figure 2*v* the presence of many large bow-shaped features on the left and the mid-latitude dark bands on the right suggest that a new Y feature may be forming upstream from the one in Figure 2*u*. In fact, 4 days after Figure 2*u*, the large distinct Y feature has been replaced by a small V shape near the morning terminator which is visible near the evening terminator the next day (Figure 2*w*). This feature appears to be displaced to the right relative to the previous feature by about 90° of longitude. Two days later (7 days after Figure 2*u*), however, a thin, distorted Y feature similar to that in Figure 2*m* appears (Figure 2*x*), requiring a 180° phase shift back to the left, as Table 2 shows. In the next several cycles the Y feature is no longer evident in the images, but many large bow-shaped features are again visible (cf. Figures 3*a* and 3*b*). This sequence of events suggests that the bow-shaped features, possibly including the dark mid-latitude bands, and the dark equatorial band can change phase or appearance to produce many different patterns and that, at times, these features fail to produce a recognizable Y feature.

The Mariner 10 imaging team interpreted this progression of tilt angles to mean that the bow-shaped features form near the subsolar point and are progressively sheared out downstream by the mid-latitude jet until small tilt angles are attained [*Murray et al.*, 1974]. However, as we have illustrated, all of the albedo features in the clouds of Venus evolve in a coordinated manner to produce a regular oscillatory sequence of tilt angle rather than a systematic trend. Certain images, such as Figures 2*b*, 2*g*, and 2*t*, show large bow-shaped features in both the morning and afternoon quadrants [*Travis et al.*, 1979*b*] and bow-shaped features with large tilt angles downstream from ones with small tilt angles. We feel that the simple shear explanation for this sequence of tilt angles is not correct, especially since the latitudinal shear of the zonal wind may not be a permanent feature of the circulation (see discussion in sections *F* and *G*).

E. IMAGE BRIGHTNESS DISTRIBUTION

In addition to the preceding subjective interpretation of OCPP images, several quantitative measures of the cloud patterns are useful. In this section we describe the OCPP imaging data by calculating (1) the moments of the cloud brightness distribution along latitude circles, (2) the longitudinal Fourier spectrum of the cloud brightness variations, and (3) time se-

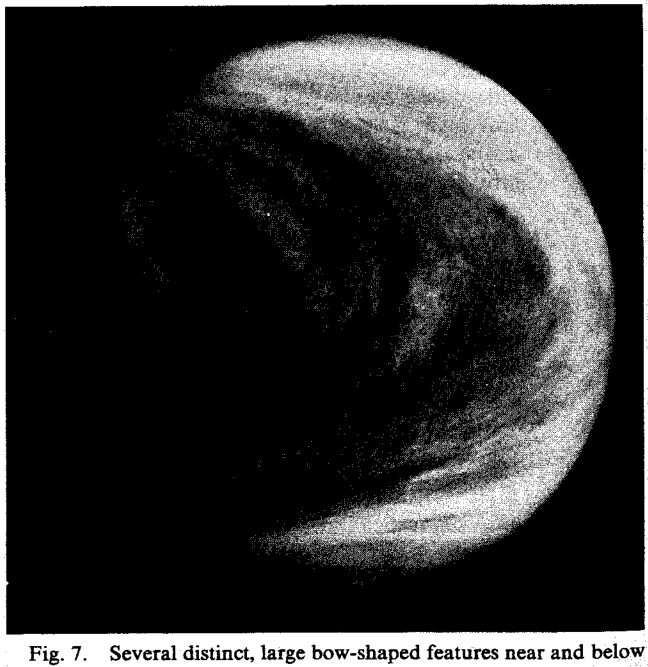

Fig. 7. Several distinct, large bow-shaped features near and below the center of the disk which are composed of cellular features (image acquired ~5 hours after Figure 3*b*).

ries of maximum image brightness, latitude of peak mean brightness, and mean brightness at selected latitudes.

1. Moments of the Brightness Distribution

We consider the first three nonzero moments of the brightness distribution along latitude circles, namely, the zonal mean, the variance, and the skewness (see Appendix A for definitions). The variance is not scale selective, but the skewness can be associated with smaller spatial scales if the spatial distribution of such features is nearly random.

Figure 12 shows the variation with latitude of the three moments of the image brightness distribution after the removal of scattering geometry variations (Appendix A). This correction primarily brightens the higher latitudes relative to lower latitudes (see discussion in section *D1*). The solid curves represent the average moments over 43 days of imaging (Table 1). They confirm the visual impression of three different types of latitude regimes, as follows:

1. The polar regions have the highest mean intrinsic brightness of any area on the planet as is evident in the raw data. The two peaks in brightness correspond to the bright polar bands near the equatorward edge of each polar region. The brightness variance is the lowest of any area, which is a reflection of the generally smooth, featureless appearance of these regions. The skewness of the brightness distribution at these latitudes is negative, which means that variations in the brightness generally appear as features darker than the mean.

2. The mid-latitude regions are characterized by a rapidly increasing intrinsic brightness with increasing latitude. In the images this trend is counteracted by the variation of the scattering geometry, which produces a decrease in apparent brightness with increasing latitude. The net result is that the mid-latitudes appear to be regions of relatively uniform intermediate brightness. The characteristic streak texture caused by the ubiquitous bow-shaped features contributes to a higher brightness variance here than in the polar regions. The small magnitude and changing sign of the skewness suggest that the mid-latitude features are composed of features both brighter and darker than the mean.

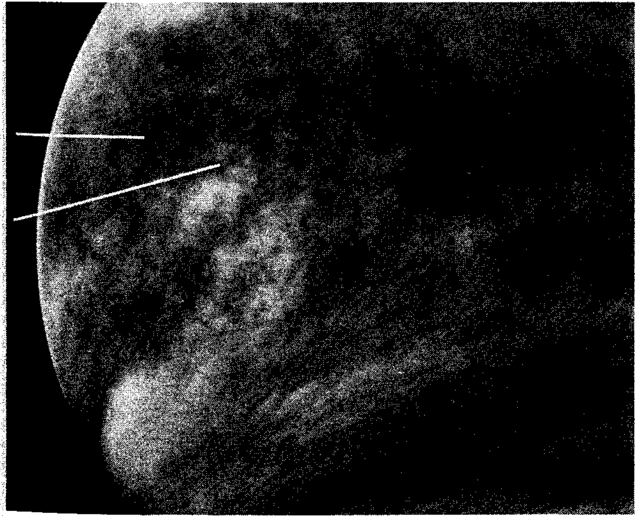

Fig. 8. Enlargement of the equatorial region in Figure 2*k* showing many cells suggestive of convective activity. The upper arrow points to a dark-rimmed cell, while the lower arrow points to a bright-rimmed cell.

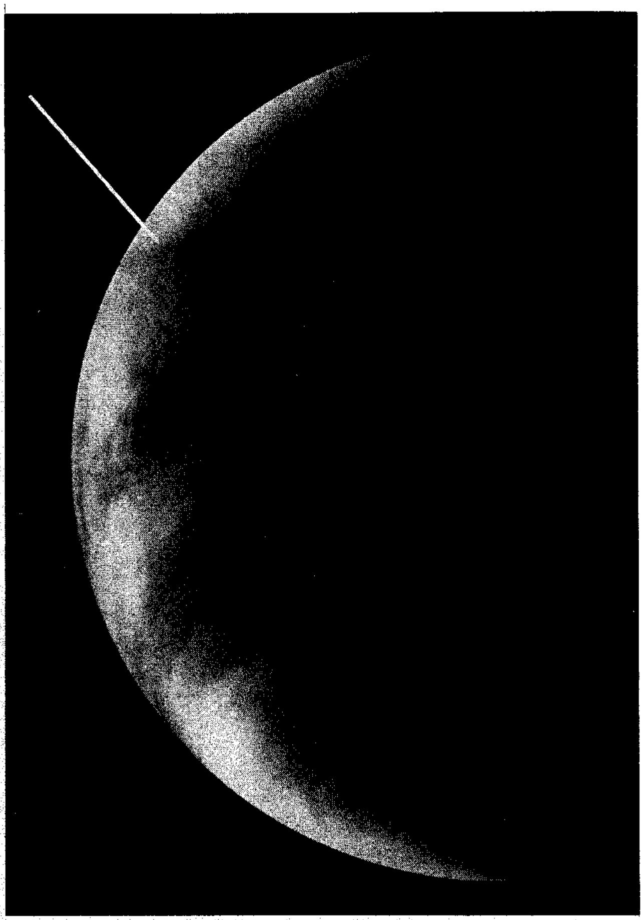

Fig. 9. The 'smoke ring' in the morning. A large bright-rimmed cellular feature (arrow) can be seen at northern mid-latitudes in this early image. The feature cuts across a boundary between a relatively dark and relatively bright region. A second faint 'ring' is visible in the original image between the primary feature and the limb.

3. The equatorial region has the lowest intrinsic brightness of any area on the planet, although the variation of scattering geometry occasionally produces the impression that this region is comparable in brightness to mid-latitudes (Figure 2*t*). The characteristic mottled texture of the equatorial region, caused by cells and the wavelike features, is reflected in the largest brightness variance of any area. The large positive skewness means that brightness variations appear as features brighter than the mean.

Qualitatively, the time-averaged brightness distribution in the images is symmetric about the equator; however, during this imaging period the mean brightness and variance of the north polar region is consistently smaller than that of the south polar region. In addition, the skewness between 30°S and 50°S latitude is much smaller in magnitude than that in the same northern latitude zone.

The other curves in Figure 12 show the brightness moments for two individual images which correspond to the two configurations illustrated in Figure 4. The moments in Figure 12*a* are from an image obtained about 5 hours after Figure 2*l* when the cloud features exhibit their maximum tilt with respect to latitude circles, the dark mid-latitude bands are present, and the dark equatorial band is absent (cf. Figure 4*a*). Since the large-scale features cross latitude circles, the zonally averaged brightness is smeared out and qualitatively resem-

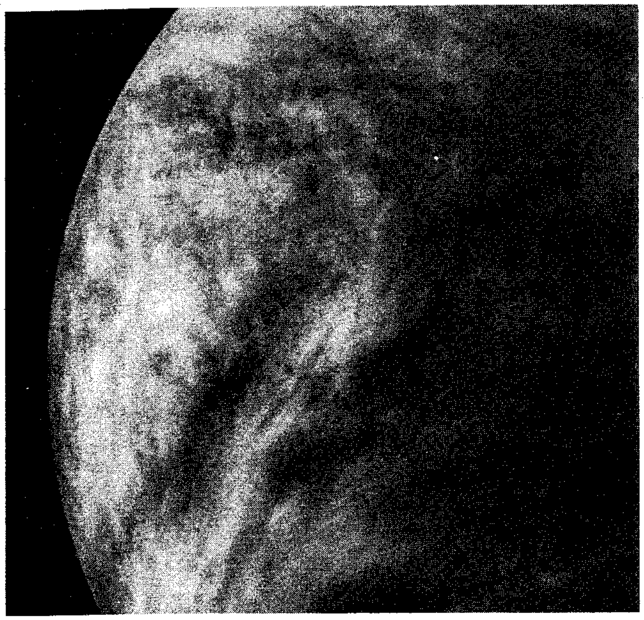

Fig. 10. Circumequatorial belts. Several bright streaks parallel to latitude circles are quite evident in the northern hemisphere (upper left) in this blowup of Figure 2*c*.

bles the time mean brightness distribution. However, the bright polar band and dark mid-latitude band in the southern hemisphere are unusually prominent in this image. This unusually large contrast is evidenced in Figure 12*a* by the larger than average variance between about 25°S and 45°S latitude. The large negative skewness in this same region reflects the presence of the dark mid-latitude band in an area with an otherwise large intrinsic brightness. The moments in Figure 12*b* are from an image obtained about 5 hours after Figure 2*r* when the dark equatorial band is present and the cloud features exhibit a more zonal alignment (cf. Figure 4*b*). The presence of the dark equatorial band is shown by the darker mean brightness at the equator in Figure 12*b*. The zonal orientation of the bright polar band accounts for the more sharply peaked brightness near 50° latitude. The local peaks in the variance and skewness near 35°S latitude probably reflect the presence of the large bow-shaped features in this image. A comparison of the polar regions in the two images suggests that the tilt of the large-scale features is primarily responsible for the variance in these regions.

2. *Spectral Analysis*

The Fourier power spectra represent the squared amplitudes of the brightness deviations from the zonal mean as a function of zonal wave number. (See Appendix A for a discussion of the calculation procedure.) The spectrum is therefore related to the variance of the brightness distribution but explicitly displays the contribution of different spatial scales. Figure 13 presents the time-averaged Fourier spectra for five latitude bands (see Table 1 for the images used). These spectra are normalized to the power at wave number 10 in the equatorial zone. In general, the power decreases with increasing latitude at all wave numbers, consistent with the decreasing variance shown in Figure 12. Over the whole wave number range (5–30), the average slope of the spectra is about −3. However, an important characteristic of all the spectra is the change in slope near wave number 10. At low wavenumbers (5–10) the slope is approximately −4, while at high wave numbers (10–30) the slope is greater than −2.5. This suggests that the cloud features are produced in two separated ranges of spatial scales, i.e., wave numbers ≤ 5 and > 30. The spectra show an obvious peak at low wave numbers (≤ 3), consistent with the predominance of global scale features in the images. There are two 'shoulders' at high wave numbers, one near wave number 12 in the equatorial zone (10°N–10°S) and one near wave number 18 in the 30°N–10°N zone. These shoulders are not present throughout the whole imaging period, however. They appear sometime after orbit number 62 (February 5, 1979) and intensify when the afternoon quadrant comes into view. Their appearance seems to coincide with the large change in the phase of the Y feature, noted in section *D3*, and with the increase of the zonal wind speed at 15°N latitude, discussed in the next section.

Travis [1978] calculated power spectra for the equatorial region and two zones in the southern hemisphere in eight Mariner 10 images. The average spectra show no peaks in the whole wave number range from 5 to 30 and a monotonic decrease of power with increasing latitude. However, these spectra show a monotonic decrease of the average slope from about −3 in the equatorial zone to about −2 in the 35°–55°S latitude zone. In addition, these spectra do not indicate any change in the slope near wave number 10.

A comparison of the spectra in Figure 13 for different latitude zones shows that the relative power at high wave numbers (> 20) decreases away from the equatorial zone, consistent with the generally more mottled texture of this region in the images. Additional calculations show a tendency for more relative power at high wave numbers when the afternoon quadrant is imaged than when the morning quadrant is imaged. These results suggest a correlation of more small-scale cloud features with low mean brightness, as suggested by the moments of the distribution and the general appearance of the images. At lower wave numbers (< 10) the two hemispheres exhibit different behavior. In the southern hemisphere the relative power decreases sharply with increasing latitude, while

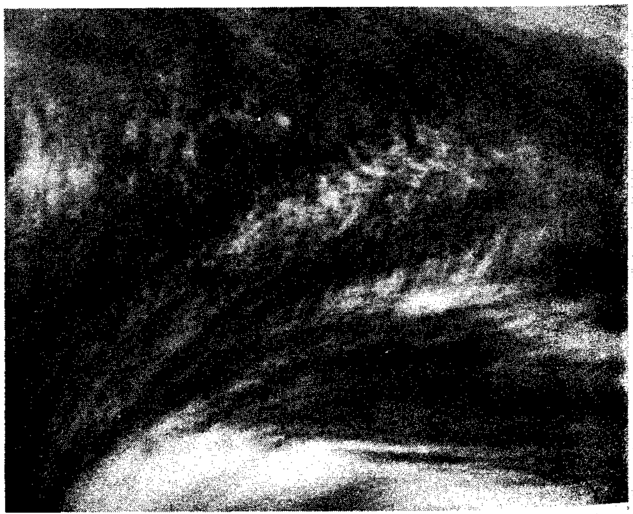

Fig. 11. Enlargement of Figure 2*x* showing the 'wave trains' in the equatorial region Alternating bright and dark streaks at a steep angle to latitude circles cover the southern mid-latitude region (right of center).

the relative power remains almost constant with latitude in the northern hemisphere. The decrease of power in the southern hemisphere for these images is somewhat greater than that exhibited by the Mariner 10 images.

3. *Time Series*

Figures 14 and 15 show some measures of the time variations of the larger-scale features over a 22-day period early in the nominal mission (see Table 1). These images have nearly identical views of both hemispheres to minimize scattering geometry effects. Figure 14 shows the variation of the zonal mean raw brightness at three selected latitudes. The middle curve demonstrates the fairly regular reappearance of the dark equatorial band every 4 days. This periodicity continues even when no Y feature is readily discernible and lends some confidence to the interpretation of phase shifts in the cloud patterns discussed previously and illustrated in Table 2.

The behavior of the polar regions is, however, much less regular. The variation of the zonal mean brightness in Figure 14 (top and bottom) shows no obvious periodicity. Likewise, the variation in the latitude of the peak zonal mean brightness (Figure 15, top and middle) shows little regularity. Despite these two facts, the variation in the maximum raw brightness for the whole image, which nearly always corresponds to a location in the bright south polar band, exhibited 10 maxima in 50 days, implying an approximate 5-day periodicity (see Figure 15, bottom). The variations of the maximum brightness on the planet and the latitude of the peak mean brightness in the southern hemisphere are weakly correlated, which suggests that the increase in maximum brightness may be produced by changes in the scattering geometry as the bright polar bands tilt equatorward. However, the weakness of the correlation argues that the explantion of these variations is more complex.

In general, the variations of the latitude of the peak mean brightness are symmetric between the two hemispheres, but some asymmetry is exhibited (Figure 15). The behavior is complicated by the fact that the variation of the brightness magnitude in the two polar regions does not seem to show any correlation (Figure 14).

F. CLOUD-TRACKED WINDS

In this section we describe the atmospheric motions in the upper cloud levels inferred from tracking the cloud features in a fashion similar to that employed for the Mariner 10 images [*Suomi*, 1974; *Limaye and Suomi*, 1980]. These preliminary results represent wind measurements on 8 sets of image triplets and 13 sets of image pairs spanning 5 weeks (see Table 1). Details of the measurement procedure are discussed briefly below and in Appendix B.

1. *Measurement Procedure*

The individual wind vectors are measured using the guided 'blind' technique, which is described and compared with a 'manual' technique in Appendix B. To provide an internal accuracy check, the vectors are measured on sets of three consecutive images acquired on the same orbit whenever possible. For this first analysis we use only full disk images because the navigation task is simpler when the entire limb is visible. Since a full disk image takes more than 4 hours to complete, the image centers in this data set are separated by about 5 hours. This separation time is 3 times longer than that used by *Limaye and Suomi* [1980], which increases the uncertainty in the wind measurements caused by changes in the cloud features (see Appendix B). In addition, the distance traversed by the faster moving features is large enough that real wind speed variations over that spatial interval may go undetected by our procedure. Later analysis of a set of partial disk images with smaller separation times will enable us to improve the estimate of the measurement uncertainty and investigate more rapid wind speed variations on smaller spatial scales.

TABLE 2. Grouping of Images in Figures 2 and 3 Into 4-Day Cycles

Cycle Number	Figure Number Day 1	Day 2	Day 3	Day 4
1				2*a*
2				2*b*
3				2*c*
4	2*d*			
5	2*e*			
6	2*f*			2*g*
7	2*h*			2*i*
8		2*j*		
9	2*k*		2*l*	2*m*
10	2*n*	2*o*	2*p*	2*q*
11	2*r*	2*s*	2*t*	2*u*
12	2*v*			
13	2*w*		2*x*	
14				3*a*
15				3*b*
16		3*c*		

We present our results as time and longitudinal average zonal and meridional wind speeds in Figure 16. The wind measurements are sorted into 10° latitude zones and the mean speed and mean latitude of all the measurements computed. The rms deviation of the individual measurements about the mean values is shown in Figure 16 by the vertical bars. This variation can be produced by measurement error, time variations of the zonal mean flow, or eddies, which are longitudinal variations of the flow. In Appendix B we estimate random measurement errors for a single wind speed value to be ~15 m s^{-1} and possible systematic errors to be ~5 m s^{-1}. The uncertainty in the mean value of a distribution of values produced by random measurement errors should decrease inversely with the square root of the number of values in the distribution. However, the rms deviations shown in Figure 16 did not change significantly when the number of values included in the average exceeded ~100 and in some cases they actually increased. This behavior suggests that actual variations of the wind speed contribute more to the deviations shown than do random measurement errors.

2. *Results*

Figure 16*a* shows the mean zonal wind speed averaged over about five weeks. The dashed curve represents the zonal wind profile that would result if solid rotation with an equatorial speed of 93 m s^{-1} obtained. Again the two hemispheres are different. The latitudinal variation of zonal wind speed in the southern hemisphere follows the solid rotation profile closely, but there are two significant deviations from this profile in the northern hemisphere. One 'jet' at about 15°N is about 10 m s^{-1} faster than solid rotation; another region of excess speed at about 45°N and an associated deficit at about 50°N are real, although their magnitudes are uncertain because of the small number of measurements.

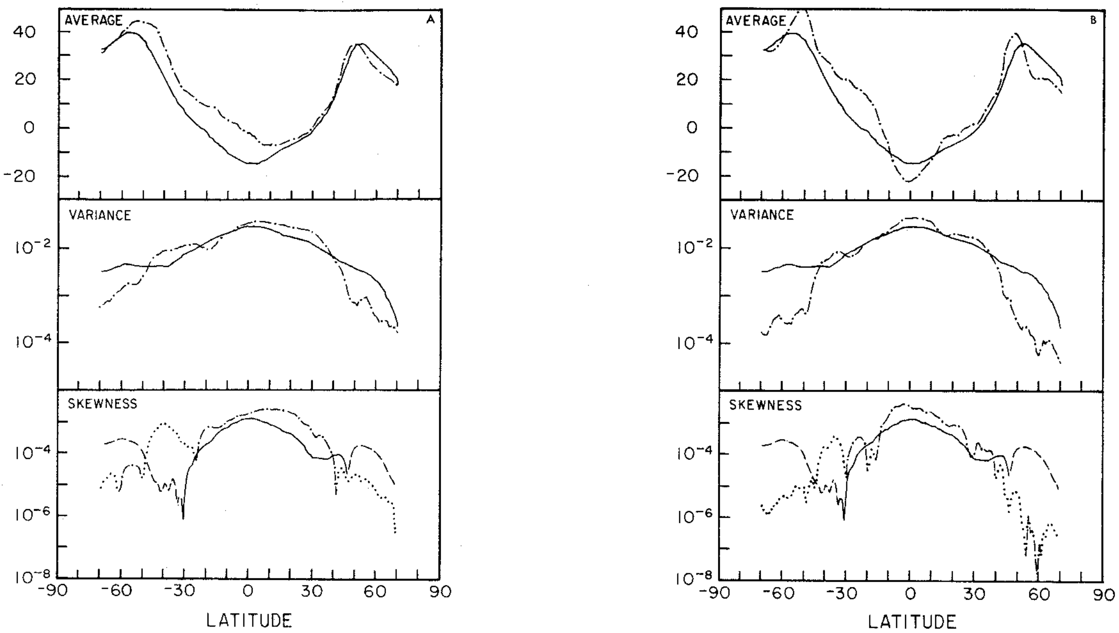

Fig. 12. Zonal mean brightness (top), brightness variance (middle), and brightness skewness (bottom) as a function of latitude for two images, (*a*) 191 and (*b*) 205, compared with the values of these quantities averaged over 27 images. For the mean and variance the solid curve represents the time-averaged values, while the dash-dot curve corresponds to the single-image values. For the skewness the solid and dashed curve denotes positive and negative values, respectively, for the time-averaged values, while the dash-dot and dotted curve has a similar meaning for the single-image values.

Figure 16*b* shows that the mean meridional wind is poleward in both hemispheres with peak magnitudes ~8 m s^{-1} in the southern hemisphere and ~17 m s^{-1} in the northern hemisphere. The hemispheric asymmetry is again striking. Tests of the sensitivity of this asymmetry of the meridional wind profile to the various sources of measurement error show that it cannot be accounted for by such errors. The cross-equatorial flow implied by Figure 16*b* could, however, be real and balanced by a return flow either at some unobserved location such as the night side or another altitude or at some unobserved time. It is also possible that the 'dynamic equator' of the circulation does not coincide with the geographic equator because the rotational constraints on the flow are weak on Venus.

A comparison of these results with those obtained from the Mariner 10 images [*Suomi*, 1974; *Limaye and Suomi*, 1980] suggests that the zonal mean circulation in the upper cloud levels on Venus is time variable. The mean meridional wind profile in Figure 16*b* is very similar to that obtained from Mariner 10 except that the wind speed maxima have apparently shifted southward by about 10° latitude. In contrast, the zonal wind profile in Figure 16*a* is very different from that of Mariner 10. The differences are emphasized in Figure 17, which shows both zonal wind profiles as angular velocity profiles. The Mariner 10 profile exhibits two strong mid-latitude jets; the OCPP profile shows a roughly constant angular velocity with two weak jets at 35°S and 15°N latitude and a stronger jet at 45°N latitude. (The angular velocity near 60° latitude in each hemisphere is rather uncertain because of the small number of measurements.)

Near the end of the 5-week period spanned by the cloud-tracked wind data, the zonal wind speed near 15°N and 35°S latitude was about 10 m s^{-1} larger than near the beginning of this period. The initiation of these increases apparently coincided with the appearance of the shoulders in the Fourier spectra of the cloud features in the 10°N–30°N latitude zone and with the large change in the phase of the Y feature discussed previously. These variations, though only slightly larger than our estimated uncertainities, could be real time variations. However, since the present image sequence varies from a view of the morning to the afternoon quadrants, another interpretation of these changes is that there is a solar-locked, standing wave in the wind field that produces this effect. More data should clarify this uncertainty. In any case, the differences between the Pioneer Venus and Mariner 10 zonal winds indicate that the actual time mean zonal flow in the upper atmosphere of Venus remains to be determined.

G. SPECULATIONS

We have only completed the first analysis of the nominal mission images. Further work on these images and planning of extended mission observations benefit from the focus provided by working hypotheses. In this section we evaluate various hypotheses about the cloud structure and dynamics near the cloud tops in the light of our results.

1. *Vertical Cloud Structure and Motions*

The OCPP polarimetry results [*Kawabata et al.*, this issue], in conjunction with the Pioneer Venus multiprobe results (if these are typical of planetary conditions), suggest that the clouds observed in the OCPP images are a complex of overlapping haze layers with different particle size modes confined to different altitude ranges [cf. *Knollenberg et al.*, this issue]. Although no complete explanation of the identity of the UV absorber(s) exists, the contrast observed in OCPP images has already provided a constraint on the vertical cloud structure. The absorber must lie within the 'main' 1-μm sulfuric acid

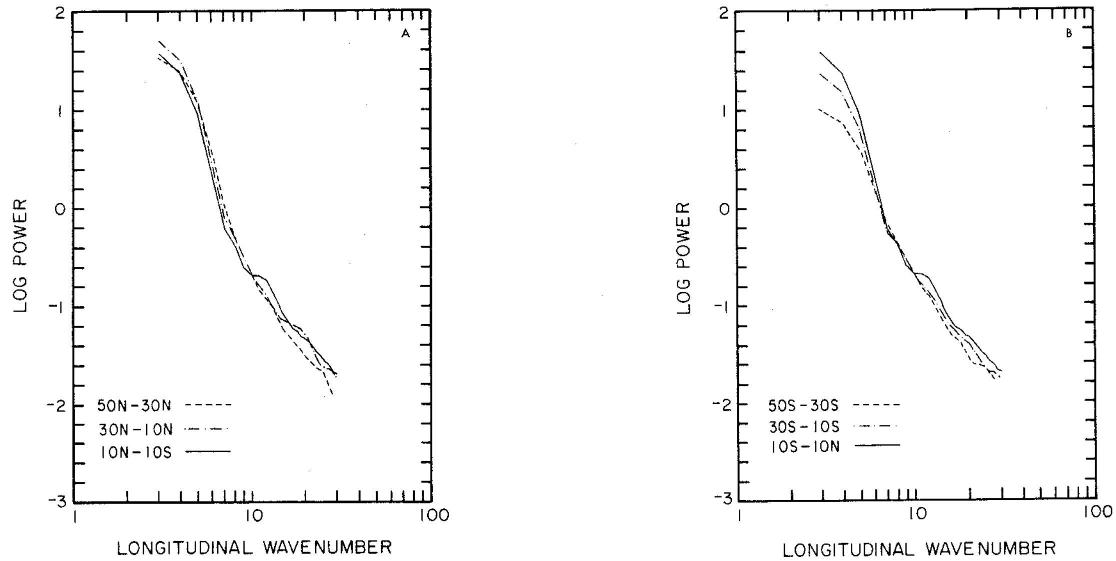

Fig. 13. Time-averaged power spectra of the zonal brightness variation for the indicated latitude bands in the (*a*) northern hemisphere and (*b*) southern hemisphere. All the spectra are normalized to the power at wave number 10 in the 10°S–10°N latitude band to emphasize relative differences.

cloud layer to produce the low contrast in high phase angle images, but not so deep that it cannot produce the rather high contrasts of the largest-scale features in low phase angle images [*Travis et al.*, 1979*a*].

We have searched our images for indications of vertical layering or indirect evidence of vertical motions. There are four such indications.

1. On the boundary between the bright polar regions and the mid-latitude regions, dark streaks occasionally appear to cut across the other features in the area (Figures 2*m*, 2*w*, 3*a*, and 6*b*). This may mean that these features are at different altitudes than the others.

2. In several images (Figures 2*j*, 2*q*, and 6*a*) bright material from the polar region appears to intrude into lower latitudes. OCPP polarimetry results show that the bright polar regions are associated with a significantly greater number density of submicron haze particles lying above the main cloud and extending more than two scale heights above it [*Kawabata et al.*, this issue]. In one comparison of a polarimetry map with an image acquired ~5 hours earlier a region of bright streamers at the northern edge of the south polar region exhibits the signature of substantial submicron haze over the main cloud. If this correlation is confirmed, it could imply that polar haze particles are being transported from the pole toward lower latitudes at these higher altitudes (see section *G3*).

3. The two types of wavelike features that have been identified suggest vertical motions in a statically stable level, i.e., gravity waves. Such a statically stable region is indicated by the probe temperature measurements above 60 km [*Seiff et al.*, this issue].

4. The cells are conceivably produced by small-scale convection. This interpretation raises two questions: (1) what process produces the large horizontal scale of these convective cells (~200–700 km) and (2) what relation do the cells have to the low static stability region observed below 60 km in the probe measurements? If the relevant vertical length scale for convection is the gas scale height, then the diameter/depth ratio of the cells may be as large as 100. Such a ratio is somewhat larger than observed in convection on earth [*Agee et al.*, 1973] and much larger than anticipated for dry convection in an unstable region. The Pioneer Venus large probe cloud particle size spectrometer experiment [*Knollenberg and Hunten*, this issue] does show a well-mixed layer in the same region of the cloud as the low stability region found by the large/small probe atmosphere structure experiment [*Seiff et al.*, this issue]. However, this level is too deep in the cloud to be observed by OCPP. One possible explanation is that the cells represent convective motions that occasionally penetrate into and spread out in the statically stable regions that are viewed by OCPP. Convection in the neutrally stable, well-mixed part of the cloud may be continuous, but perhaps only a few cells are vigorous enough to penetrate to higher altitudes.

One common 'explanation' of the dark UV features is that they are produced when convective motions bring dark material up from below which is then distributed into planetary scale features by the winds aloft. This picture is not supported by the observed interactions of the large-scale features with the cells. If numerous cells produced a dark albedo feature, then we should observe a permanent, sun-locked, large-scale dark feature near and downstream from the subsolar point. Although the Mariner 10 imaging team concluded that this region was disturbed [*Murray et al.*, 1974], they and we do not see any evidence for a sun-locked dark feature. As discussed in section *D2*, the dark equatorial band is a common feature, but it propagates around the planet, appearing fully formed even at the morning terminator (Figure 2*a*), where fewer cells are seen.

2. *Horizontal Cloud Structure and Motions*

The bow-shaped features observed in the OCPP images can be more than 10,000 km long and yet only 500–1000 km wide (e.g., Figure 3*a*). On some occasions they move across the disk as a single unit and reappear in an altered but recognizable form 4 days later (e.g., the arms of the Y feature in Figures 2*q* and 2*u*), suggesting a lifetime >4 days. Yet the same features can completely disappear in less than 4 days (Figures 2*u* and 2*w*) rather than slowly decaying away. Furthermore, other

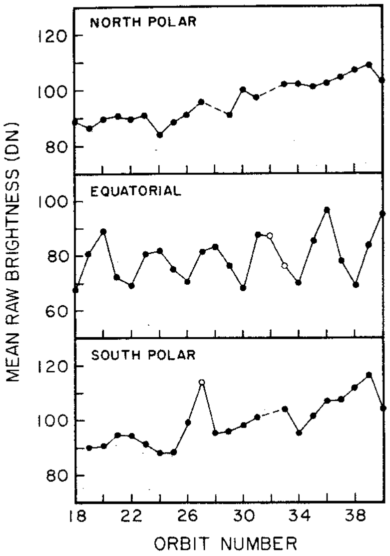

Fig. 14. Variation of zonal mean raw brightness for scan lines in the north polar region (~50°N, top), equatorial region (~0°, middle), and south polar region (~50°S, bottom) as a function of time. Dashed lines indicate gaps in the data coverage, while open circles represent data from within 5° of the desired latitudes for images where those data are missing.

features, such as cells, which are about the same size as the smaller dimension of the bow-shaped features, consistently exhibit lifetimes <1 day and often as short as ~5 hours and yet change orientation in a globally coordinated manner to produce the characteristic V-shaped pattern. (This behavior is further discussed in section *G3*). These interpretations of the images, taken together, describe a puzzling combination of very different length and time scales in the same feature, which is a challenge to any explanation of them.

One suggestion for the production of these particular features is that they are produced as localized dark regions and then sheared into long thin streaks by the mean meridional and zonal winds. In addition to the problem of the source region of the dark material discussed above, this explanation cannot account for the large tilt angles regularly seen in the images, since the zonal mean meridional winds are at least an order of magnitude smaller than the mean zonal winds. Furthermore, the evolution of the tilt angles described in section *D3* argues against shearing motion. The near solid rotation zonal wind profile in the southern hemisphere suggests that the mid-latitude jets and the associated shear are not constant features of the zonal flow and cannot be the sole reason for the tilted orientation of the cloud features.

The difference between the regular 4-day oscillation of equatorial brightness (Figure 14) and the ≥ 4.5-day average rotation period obtained from the cloud tracked winds (Figure 17) suggests that the large-scale cloud features are associated with propagating wave motions. *Belton et al.* [1976*a*, *b*] proposed that the Y feature is the manifestation of two linear types of planetary scale waves with phase speeds which counteract the shear of the zonal wind observed by Mariner 10. Although the Y feature appears to be a composite structure, its existence during periods of both negligible and substantial shear in the zonal wind suggests a more complex situation. *Rossow and Williams* [1979] showed that a single nonlinear planetary scale wave can also produce a coherent perturbation pattern that moves without distortion even in the presence of mid-latitude jets as a natural consequence of quasi-two-dimensional interactions of the waves and mean flow in a slowly rotating atmosphere. This result solves the problem of the varying shear and accounts for the predominance of wave number 1 in the images, but it does not readily explain the characteristic tilted orientation of cloud features or the presence of the dark equatorial band. Neither of these proposals tried to account, moreover, for the small time and length scales evidenced by the bow-shaped features in the OCPP images.

We propose that the smaller time and length scales, though not the characteristic orientation of the large-scale cloud features, can be accounted for if the UV albedo features in the Venus clouds are produced by a large-scale modulation of the relative contrast of ubiquitous small-scale features. In other words, two well-separated scales of motion are present in the upper cloud levels on Venus, with smaller-scale features such as the cells and short mid-latitude streaks acting as tracers of the planetary scale wave motions. (However, even if the contrast of the small-scale features is modified by the large-scale motions, the small-scale features' motions would still reflect the actual wind velocities.) This explanation is consistent with four properties of the cloud albedo features identified in the OCPP images.

1. The time-averaged power spectra of the albedo patterns (Figure 13) show relatively more power at both low and high wave numbers than at intermediate wave numbers when compared to a spectrum with constant slope. The length scale of the cells and small bow-shaped features (wave number ~50) is not resolved in these spectra (cf. discussion in Appendix A), but the slope of the spectrum at wave numbers >20 is consistent with the visual impression produced by the images. In particular, the slope decreases going from high to low latitudes and from the morning to evening terminator region (de-

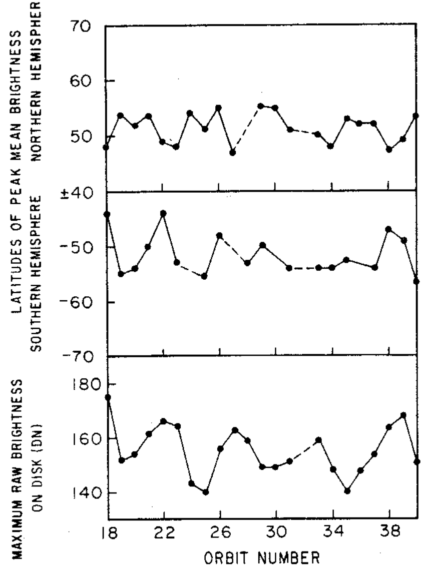

Fig. 15. Variations of polar properties on successive orbits of the spacecraft. The top two curves show the change in latitude of the maximum zonal mean brightness as a function of time. The bottom curve shows the variation of the maximum raw brightness on the whole disk as a function of time. Dashed lines indicate gaps in the data coverage.

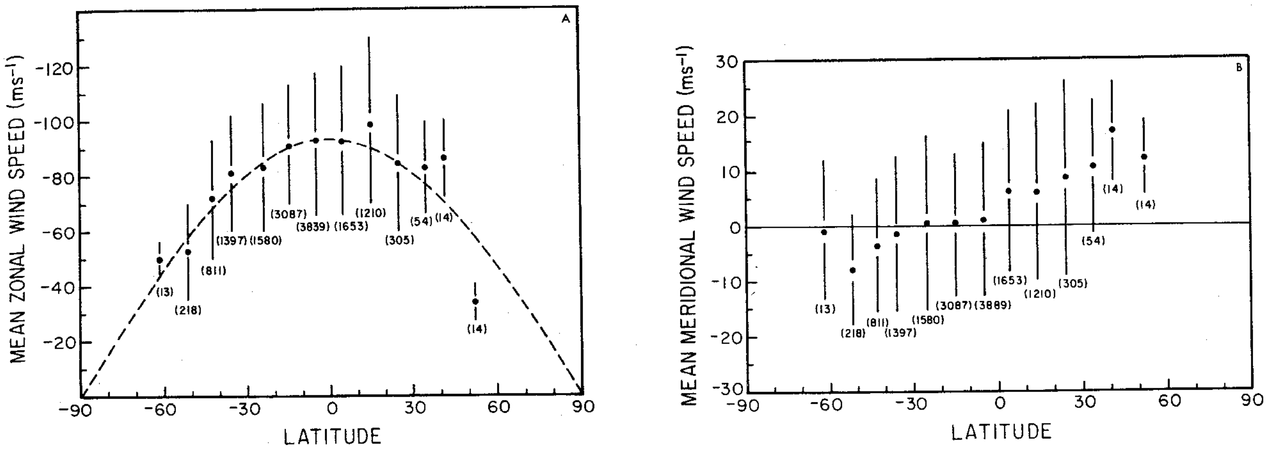

Fig. 16. (*a*) Time and longitudinally averaged zonal wind speed and (*b*) meridional wind speed as a function of latitude obtained from tracking ultraviolet cloud features. The dashed curve in Figure 16*a* represents the latitudinal variation of zonal wind speed corresponding to solid body rotation. The number of wind vectors averaged to produce each value is indicated by the numbers in parentheses. The vertical lines indicate the rms deviation of the measurements about the mean.

termined from spectra of images showing predominantly one quadrant), that is, from regions with less to regions with more mottled appearance. Consequently, we believe that these spectra reflect the presence of the two scales of motion required by our interpretation.

2. Large-scale modulation of feature contrast is suggested by a comparison between the morning and evening terminator regions. Large bow-shaped features are sometimes visible near the morning terminator (Figure 2*c*), but they are generally more obvious in the evening terminator region (Figure 3*a*). The same is true of the cells. This longitudinal asymmetry may reflect processes which occur preferentially in the afternoon quadrant, but we favor the alternative explanation that this asymmetry reflects a large-scale modulation of the contrast of ubiquitous small-scale features. The polarimetry results indicate an increase in the amount of high-altitude submicron haze near the morning terminator [*Kawabata et al.*, this issue], suggesting that the lower contrast here is caused, in part, by local increases in the amount of UV scattering material above the UV absorbing material, but some additional modulation is required to explain the total effect. When the dark equatorial band is present in morning quadrant images, the brightness variance increases and more small-scale structure is evident (Figure 2*a*). These facts argue against the simple absence of all small-scale features in the morning terminator region.

3. Our examination of the OCPP images leads us to believe that the spatial distribution of the small-scale features at low and middle latitudes is essentially random. If this is true, then these features control the skewness of the brightness distributions of these latitudes. If, in addition, the small-scale features exhibit a very broad range of brightness (as suggested by the large variance), then the large-scale modulation of the brightness of such small-scale features to produce an increase of the mean brightness with increasing latitude would cause the observed change in the skewness from positive to negative.

4. The strongest evidence for our hypothesis is the regular variation in the tilt angles of the cloud features, even the smaller ones, over the whole planet, discussed in section *D3*. Figure 4 illustrates the two extremes of this variation when the dark equatorial band is absent (Figure 4*a*) and present (Figure 4*b*).

The puzzling combination of length and time scales in a single feature and the planetary coordination of the feature orientation can be explained if a background of short-lifetime, small-scale features acts as a 'dye marker' of a larger-scale motion field. The rapid changes in appearance of parts of a large-scale feature can then be attributed to a change in the 'tracers' rather than to a change in the large-scale feature. The individual, short-lived cumulus clouds in a mid-latitude cyclonic storm on earth behave in just this fashion, for example. Even though the Y features in Figures 2*q* and 2*u* appear similar, the detailed, small-scale structure is very different and composed, we propose, of entirely different features. The relationship is actually more complicated, as illustrated by occasional examples of large bow-shaped features composed of a chain of cells (Figure 7) or cells clustering along the dark mid-latitude bands (Figure 2*i*). These images suggest a nonlinear interaction between the two scales of motion. This interaction could account for the variable relationships between the small- and large-scale albedo patterns which result in rapid changes in the Y feature (e.g., Figures 2*m* and 2*q*) and occasionally cause the disappearance of the Y feature.

3. *What Causes the Cloud Albedo Patterns?*

The above speculations about the evolution of the UV cloud albedo patterns are carefully phrased to avoid suggesting any particular process which produces the small-scale albedo perturbations and the large-scale modulation of them. Until we can identify the UV absorber(s) as a gas, a separate aerosol, a contaminant in the sulfuric acid aerosol, or some combination of these possibilities, we cannot really place any confidence in explanations of the albedo variations. However, current knowledge about the structure of the upper sulfuric acid cloud places some constraints on its role in any proposed explanation.

1. If the sulfuric acid particle properties and the mean cloud structure are in a steady state, then the time constants for particle growth and particle removal from the cloud must be equal. The observed 1-μm particle scale height, about half

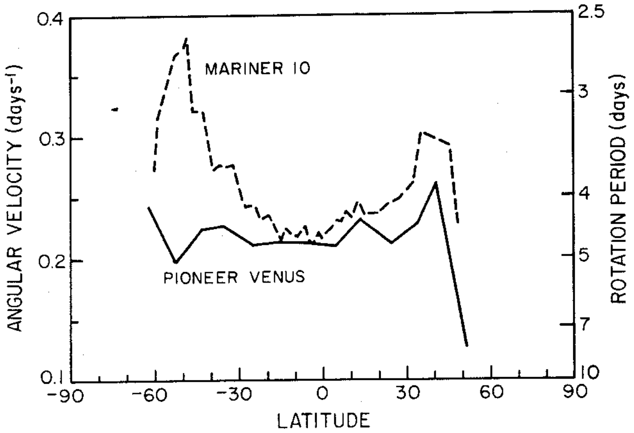

Fig. 17. A comparison of angular velocity profiles obtained from the OCPP cloud-tracked winds in Figure 16*a* and Mariner 10 cloud-tracked winds measured by *Limaye and Suomi* [1980].

the gas scale height [*O'Leary*, 1975; *Lacis*, 1975], limits the possible turbulent vertical transport and means that the removal time must be $\sim 10^7$ s, regardless of where the particles are produced [*Rossow*, 1977, 1978]. It is unlikely that freezing sulfuric acid can change its optical properties enough to explain the albedo changes; thus the rapid variation of the albedo pattern, especially on small length scales, cannot be explained by changes in the main sulfuric acid cloud properties or distribution.

2. The sulfuric acid cloud is very tenuous; the levels above about 65 km are similar in density to typical urban smogs. The physical thickness of this cloud required to give an optical thickness ~1 is roughly half an atmospheric scale height (~2 km). Thus even though the cloud features we observe in the images involve rather small contrasts (≤ 30%), the changes in the cloud properties that produce them probably occur over a substantial altitude interval. Preliminary examination of the polarimetry data shows no qualitative differences in the polarization between dark and bright regions [*Kawabata et al.*, this issue]. (The exceptions to this statement are the bright polar regions which are discussed below.) This result means that large changes in the uppermost (>70 km) levels of the sulfuric acid cloud are not involved in producing the UV cloud features.

3. The submicron haze detected by the OCPP [*Kawabata et al.*, this issue] provides additional scattering optical depth, but it cannot completely explain the variations in UV albedo, especially if it is composed of sulfuric acid [*Knollenberg et al.*, this issue], for three reasons: (1) there is not enough of it at lower latitudes to produce the observed contrasts there, even though the amount of haze during this imaging period is much greater than usual, (2) it is difficult to move these particles relative to the 1-μm particles except by sedimentation, which takes $\sim 10^7$ s, and (3) a similar time scale constraint, as discussed in explanation 1 above, applies to these smaller particles as well.

4. If the haze is not sulfuric acid (cf. *Knollenberg et al.* [this issue] for arguments against this proposition), it could certainly be a condensate, which would alleviate the time constant problems. However, if the haze is a UV scattering material, it has the same difficulty producing the low-latitude contrasts as sulfuric acid. The haze cannot be the UV absorber or else the poles and the high phase angle, morning terminator images would be dark with high contrast, not bright with low contrast [*Travis et al.*, 1979*a*].

5. The short lifetimes of small-scale features and the variation of the amount of haze above the main cloud could be interpreted to mean that the sulfuric acid particle properties and cloud structure are not in steady state but rather in a vacillating equilibrium [*Rossow*, 1978]. In this case, the sulfuric acid particles could be growing at much faster rates, consistent with the short variation time scales. However, the amount of submicron haze needed to produce the observed magnitude and time variation of the small-scale constasts at low latitudes implies a mass injection rate at upper levels which greatly exceeds the inferred removal rate. A vacillation of the polar cloud structure on longer time scales ($\geq 16^6$ s) is possible, nevertheless.

One example of a UV albedo variation which can be related to a change in cloud structure is the polar brightening in 1979. This brightening is a consequence of the presence of a thick submicron haze over the 1-μm main cloud [*Kawabata et al.*, this issue]. These observations further imply that on a constant pressure surface going from low to high latitudes the number density of 1-μm particles decreases and that of haze particles increases. These observations lead us to propose that polar brightening events are produced by the following sequence of events. In the absence of eddy mixing, the 1-μm cloud settles out at the pole relative to that at the equator because the latter is supported by the weak vertical flow of the meridional circulation. If haze particles are produced primarily in the polar regions above the 1-μm cloud, then a buildup of submicron haze will brighten the pole when eddies are not active. When planetary scale eddies become active and exchange polar air with equatorial air along isobaric surfaces, they darken the pole by adding 1-μm particles and removing submicron haze particles. This explanation is consistent with the inferred advection time scales (see below) and the variability time scale of the polar brightness changes [*Dollfus*, 1975].

4. *Dynamics of the Upper Cloud Levels*

Several characteristics of the UV albedo variations and the cloud-tracked wind analysis, together with recent theoretical studies, lead us to propose, as a working hypothesis, that our data support *Gierasch*'s [1975] model of the so-called 4-day wind. In this model the mean meridional (Hadley) circulation of the Venus atmosphere, driven by the equator-to-pole radiative heating contrast, is responsible for transporting a fraction of the angular momentum of the lower atmosphere into the upper atmosphere. The lower atmosphere obtains its angular momentum through frictional interaction with the solid planet, and the Hadley circulation transports some of this momentum upward if the poleward branch of the circulation does not conserve angular momentum. The latter effect was modeled by *Gierasch* [1975] as a strong horizontal momentum diffusion. *Kalnay-Rivas* [1975] showed that such a parameterization for diffusion implies such a strong heat diffusion, even for Prandtl numbers as large as 100, that the Hadley circulation is suppressed. (We note that Gierasch explicitly neglected horizontal heat diffusion in his model equations.) However, *Rossow and Williams* [1979] proposed that with a large static stability and small horizontal temperature contrasts in the upper atmosphere of Venus the eddy motions would be quasi-barotropic and quasi-nondivergent. They were able to show that if the forcing of the flow were weak enough, such quasi-two-dimensional eddy interactions would provide the proper momentum transport to complete Gierasch's model without transporting any heat, since the eddies are barotropic. The criterion for weak forcing is that the advective time scale of the mean circulation be much larger than that for the redistribution of momentum by the eddies ($>10^6$ s).

The Mariner 10 and preliminary Pioneer Venus OCPP results, taken together, lead us to suggest that the above processes operate to produce a cyclic variation of the flow in the upper Venus atmosphere. If we start from a state of solid body rotation, then the poleward branch of the mean meridional overturning will transport angular momentum poleward and build up a mid-latitude jet. As the jet grows stronger, it will become barotropically unstable. Eddies will develop and transport angular momentum equatorward, and the flow will relax back to the original state of solid body rotation. Over a long time the repetition of the cycle could supply enough angular momentum to the upper atmosphere to maintain the 4-day wind. Such a vacillation cycle is consistent with all of the following observations from Mariner 10 and Pioneer Venus.

1. The southern mid-latitude jet inferred from the Mariner 10 imaging does not appear in our nominal mission imaging and the northern mid-latitude jet is much weaker (Figure 17). This suggests that the jets are not permanent features of the circulation. Since the magnitude of the deviation of the zonal flow from solid rotation is an approximate measure of its relative stability [*Rossow and Williams*, 1979], the southern mid-latitude jet in the Mariner 10 data is much less stable [*Travis*, 1978] than the southern hemisphere zonal flow in our data. Further, the southern hemisphere mean zonal flow in the nominal mission images is nearly that of solid body rotation, the relaxed state produced by two-dimensional eddy interactions [*Rossow and Williams*, 1979].

2. Since the radiative heating of the Venus atmosphere is symmetric about the equator, the mean meridional circulation that it drives is expected to be symmetric also. The observed asymmetry of the mean zonal and meridional flows requires the presence of motions not directly forced by radiation. Since the barotropic instability of zonal flows can produce antisymmetric eddies [*Baines*, 1976], this process may account for the observations.

3. If the cloud brightness distribution Fourier spectrum is interpreted as the eddy kinetic energy spectrum of the circulation, the Mariner 10 data [*Travis*, 1978] and our own generally show a slope close to -3 in the equatorial region, corresponding to the relaxed two-dimensional turbulent regime. (The slopes are calculated, as described in Appendix A, for the wave number range between 5 and 20.) At mid-latitudes, on the other hand, our spectra also show a -3 slope, but the Mariner 10 mid-latitude spectrum, corresponding to the location of the jet, has a slope near -2 [*Travis*, 1978]. The latter slope implies generation of kinetic energy at higher wave numbers, as could be the case if barotropic instability is occurring. Further evidence of this type of correlation is the appearance of shoulders in the spectrum in the 10°N–30°N latitude zone at about the same time as an increase in the 15°N jet speed.

4. The hemispheric mean meridional velocity in our data is $\sim$2–6 m s^{-1}, which implies a momentum advection time scale $\sim 5 \times 10^6$ s. The time scale is consistent with our explanation of the change in altitude of the 1-μm cloud particles and the submicron haze particles between the equator and the pole, i.e., that the changes are due, in part, to the sedimentation of the 1-μm particles relative to the haze particles during poleward advection with a time scale $\sim 10^7$ s. This momentum advection time scale also places these motions in the weakly forced regime described by *Rossow and Williams* [1979]. *Gierasch* [1975] estimated the meridional overturning time scale by assuming a thermal balance between adiabatic cooling and radiative heating. He obtained $\sim 10^7$ s for this time scale, consistent with these results.

Although nothing in our results yet precludes the alternative wave transport or Reynolds stress explanations of the vertical momentum transport (see *Stone* [1975] for a review), these theories do not provide any explanation for the other phenomena that we do observe. Consequently, we believe that our results are consistent with the interpretation that the mean meridional circulation/barotropic eddy processes are producing the 4-day wind in the upper cloud levels on Venus. Of course, we have analyzed only about 5 weeks of images, and the use of a few weeks of data separated by 5 years to elucidate atmospheric processes with time scales of $\sim$100–1000 days is hardly definitive. In addition, we do not observe the vertical structure of the wind fields below the clouds. Nevertheless, these preliminary results do suggest that the momentum balance in the upper atmosphere is not a steady state balance but rather a vacillating equilibrium. This conclusion seems also to apply to the abundance of submicron haze lying above the cloud and the associated polar brightening, to the globally averaged, cloud top pressure [*Coffeen and Hansen*, 1974], and to the radiative-thermal balance [cf. *Tomasko et al.*, this issue]. It is clear from the differences between the Mariner 10 observations of the upper atmospheric dynamics and our own that whatever the explanation of the Venus winds, data obtained over an extended time base will be necessary to define the general circulation and to diagnose the processes which maintain it.

H. SUMMARY

The definite conclusions which we have reached are listed here.

1. The overall brightness distribution of the clouds in the Pioneer Venus OCPP images differs from that in the Mariner 10 images in that the polar regions are significantly brighter.

2. In addition to the albedo features identified in the Mariner 10 images one new type of small-scale wave feature has been identified in the Pioneer Venus images. We confirm the concentration of the large bow-shaped features and small cell features near and downstream of the subsolar point at latitudes between ±20°, but we also observe both types of feature in the morning terminator region, in contrast to the Mariner 10 observations. The classical dark Y feature appears quasi-periodically every 4 or 5 days but occasionally disappears for several cycles. The most important observation is that all of the albedo markings exhibit a planet-wide, coordinated, regular, oscillating evolution of their orientation relative to latitude circles whether a Y feature is evident or not.

3. The measured mean meridional wind velocity agrees with the Mariner 10 results in both direction (poleward in both hemispheres) and rough magnitude. The mean zonal wind speed agrees with the Mariner 10 results, giving a rough 4–5 day retrograde rotation of the cloud features; however, the latitudinal profile in the Pioneer Venus images differs significantly from that obtained from Mariner 10 images.

The most important conclusion drawn from a comparison of Mariner 10 and Pioneer Venus results is that the cloud structure and atmospheric motions on Venus can and do change significantly with time and that data collected over a long time period, at least ~100–1000 days, will be required to describe the general circulation of this part of the Venus atmosphere.

APPENDIX A

Image Normalization

The images chosen for the objective brightness distribution studies were acquired at times when the telescope look angle, measured relative to the spacecraft spin axis, was close to 90°. The subspacecraft latitude at the center of these images is within 10° of the equator (see Table 1), and as a result, scan lines can be assumed to be roughly parallel to latitude circles. With this assumption the latitude corresponding to a given scan line can be estimated from a knowledge of the total number of scan lines on the disk. The longitude for each pixel, relative to the subsolar meridian, is then calculated by using information on the total number of pixels on the disk for each scan line, the phase angle at the disk center, the apparent angular diameter of the disk, and the longitude of the subspacecraft point.

The images are normalized to remove the effects of variable scattering geometry over the disk. The first step is to calculate a solar zenith angle θ_n for each pixel from the estimates of latitude and longitude. A disk-integrated normalized intensity I_D is then calculated using the assumption of Lambertian diffuse reflection:

$$I_D = \sum_n I_n^{\text{raw}} \left[\sum_n \cos\theta_n \right]^{-1} \qquad \text{(A1)}$$

where I_n^{raw} is the raw intensity for pixel n and the sum is over the entire disk. Finally, the normalized intensity I_n for pixel n is determined by subtracting the intensity of the Lambert sphere at the appropriate zenith angle from the raw intensity:

$$I_n = I_n^{\text{raw}} - I_D \cos\theta_n \qquad \text{(A2)}$$

The normalized intensities are thus an indication of intrinsic brightness deviations from the mean brightness over the disk; they can have positive or negative values, corresponding to relatively bright or dark features, respectively, and they collectively sum to zero over the entire disk. For any single scan line, though, the average of the I_n is, in general, nonzero.

Lambert's law is a crude basis for normalization, since it is independent of the observer viewing angle. Consequently, I_D will vary from image to image because of the changing phase angle, independently of any intrinsic time variations in the UV albedo of Venus. However, for the purpose of illustrating relative contrasts between features in a particular image, Lambert's law gives qualitatively the same results as a more exact normalization scheme, for example, one using the Chandrasekhar H functions [*Limaye and Suomi*, 1977].

Moments of the Brightness Distribution

Using the normalized intensities at each 1° of longitude I_m, we calculate the first three nonzero moments of the brightness distribution along each scan line:

$$\bar{I} = \frac{1}{m} \sum_m I_m \qquad \text{(A3)}$$

$$\bar{\sigma}^2 = \left[\frac{1}{m} \sum_m (I_m - \bar{I})^2 \right] \Big/ (\bar{I} + I_D)^2 \qquad \text{(A4)}$$

$$\bar{\chi} = \left[\frac{1}{m} \sum_m (I_m - \bar{I})^3 \right] \Big/ (\bar{I} + I_D)^3 \qquad \text{(A5)}$$

where the sum is over longitude. We express the second and third moments of the distribution as a fraction of the mean total brightness, $\bar{I} + I_D$; e.g., $\bar{\sigma}^2 = 10^{-2}$ is equivalent to an rms brightness deviation 10% of the total mean brightness. Although the definitions in (A4) and (A5) are not the standard definitions of the variance and the skewness, respectively, we will use these terms for convenience. The standard variance and skewness can easily be found from the values of $\bar{I}$, I_D, $\bar{\sigma}^2$, and $\bar{\chi}$, however.

The mean brightness $\bar{I}$ defined in (A3) represents the deviation of the mean brightness of a scan line from the disk-integrated brightness and can be either positive or negative like I_m. The variance $\bar{\sigma}^2$ is the mean squared amplitude of brightness variations on all length scales along the scan line. The skewness $\bar{\chi}$ is a measure of the asymmetry about the mean of the brightness distribution along a scan line. Skewness is controlled by those locations at the extremes of the brightness distribution, and its sign indicates whether there are more locations brighter (positive) or darker (negative) than the mean. Usually the number of such locations is smaller than those nearer to the mean in brightness. Thus, if the brightness distribution is spatially random, the skewness can be controlled by small-scale features.

Power Spectrum Analysis

The first step in calculating the longitudinal power spectrum is to map the normalized intensities I_n for each scan line into an array $I(\phi_n)$ with one point per degree of longitude ϕ. Pixels near the limb are excluded from the analysis in order to reduce foreshortening effects; the criterion used is that there must be at least one pixel per degree of longitude. Only images with phase angles <35° are used, since we wish to have data from as much of the sunlit side of the planet as possible. The combined effects of the foreshortening, the finite angular diameter of the disk, and the partial illumination of the disk in the images limit our data set to a maximum of ~155 points at the equator at the lowest phase angles. This maximum decreases with increasing latitude to ~145 points at 50° latitude because of decreasing angular resolution. It also decreases with increasing phase angle because a smaller fraction of the disk is illuminated. (For example, the maximum is ~125 points at 35° phase angle.) In order to reduce any systematic latitudinal bias resulting from the variation of the length of the longitudinal sector we restrict our data set to the same number of points at all latitudes in a given image (145 at low phase angles, decreasing to 125 at the higher phase angles). Spectra are not presented here for latitudes poleward of 50° because the foreshortening is too severe. However, it should eventually be possible to extract information on the 50°S–70°S latitude band by analyzing images with better views of the southern hemisphere.

Spatial scales of the brightness variations along a latitude circle (in this case, a scan line) are represented by longitudinal planetary wave numbers, which are equal to 360° divided by the wavelength in degrees longitude of the corresponding Fourier component. The finite spatial resolution of this data set introduces spurious power at all wave numbers. This effect, called aliasing, increases in importance with increasing wave number until half of the power is spurious at a wavelength twice the discrete resolution element in the data. The corresponding wave number, the Nyquist wave number, is the highest wave number (smallest spatial scale) that is resolved by the data. Our 1° longitude resolution implies a Nyquist planetary wave number of 180, so aliasing contributes no more than 1–2% to the power at wave numbers ≤ 30.

The truncation of the length of the longitude sector covered by our data at less than 360° introduces a more important source of spurious power. In order to analyze the brightness distribution on a limited sector in terms of planetary wave numbers we must assume some brightness in the sector not covered by our data. This assumption produces changes in the power spectrum at all wave numbers because of the discontinuity at the ends of the data sector. Some additional treatment of the data to reduce this effect is possible, however. (Although the spurious power introduced by the particular analysis used here limits our spectra to wave numbers ≤ 30, this is not a fundamental limitation of the data.)

First, we subtract the scan line average brightness from each data point, so that the new intensities represent deviations from a zero mean, and we assume that the brightness of the remainder of the latitude circle is zero [*Travis*, 1978]. We then 'prewhiten' the data, following a suggestion by *Holloway* [1958]:

$$I'(\phi_n) = I(\phi_n) - 0.75I(\phi_{n-1}) \tag{A6}$$

The purpose of this procedure is to amplify high wave number components and flatten the spectrum before Fourier analysis. This reduces instability in making spectral estimates caused by the large amount of power at low wave numbers as compared to high wave numbers. After the power spectrum is calculated, we can correct for the prewhitening by dividing by the square of the frequency response $R(k)$ of the prewhitening operation (A6):

$$R(k) = 1.5625 - 1.5 \cos (2\pi k/L) \tag{A7}$$

where k is the longitudinal wave number and $L = 360°$. Finally, we multiply the data by a function which goes to zero at the endpoints to minimize the effects of the discontinuities there. The function used is the hanning function [*Blackman and Tukey*, 1958], defined by

$$H(\phi_n) = \tfrac{1}{2} - \tfrac{1}{2} \cos (2\pi\phi_n/N) \tag{A8}$$

where N is the number of points in the data set. The result of this operation is a modified data set $B(\phi_n)$:

$$B(\phi_n) = I'(\phi_n)H(\phi_n) \tag{A9}$$

This last step produces a systematic underestimate of the power in the lowest resolved wave numbers.

The power spectrum is obtained by calculating the squared amplitude of the Fourier transform of this modified data set for each scan line. This is done successively in steps of 1° latitude, and the resulting spectra are averaged logarithmically over latitude bands of 20° width to reduce further the effects described above. Finally, the spectra are again averaged logarithmically over a set of 27 images covering 43 days roughly centered on the time of zero phase angle (Table 1). This eliminates the effects of transients and gives a better statistical sampling of the time-averaged behavior of Venus cloud brightness features.

The longitudinal length of the data set restricts the spectra to wave numbers 3 and greater. Tests on artificial data sets with power law spectra indicate that the foregoing procedure gives reliable estimates for wave numbers 5–30 when a number of spectra are averaged. Calculations of terrestrial kinetic energy spectra using observed winds over 180° longitude [*Julian et al.*, 1970] and cloud brightness over ~90°–160° longitude [*Travis*, 1978] also support this claim. We estimate that the slopes of the power spectra, calculated by a least squares linear fit to the spectral estimates at each wave number, are accurate to within ~±0.5.

APPENDIX B

Wind Velocity Measurement Procedure

The wind velocities reported in this paper are obtained by tracking cloud motions in the OCPP images using a guided blind tracking technique. The displacement of a cloud feature between two consecutive images is measured by calculating the cross-correlation matrix between a field of 32 × 32 image elements (pixels) selected arbitrarily from the first image and a 65 × 65 pixel 'search' field in the second image. The peak correlation, if it does not occur on a boundary of the search field, is taken to be the position of the cloud feature in the second image. To reduce the computing time required for each measurement of a displacement, the location of the center of the search field is predicted from the coordinates of the cloud feature in the first image and the displacements measured on other image pairs. The search area is large enough, however, that the measured velocities are only constrained to ± 50 m s^{-1} about the predicted value. The wind velocities are then obtained by dividing the displacement vector by the time separating the images.

Measurement Errors

The two primary sources of error in measuring cloud feature displacements are the determination of the location of the pixels in the images in a reference coordinate system, called image navigation, and changes in the shape and size of a cloud feature during the time between images. Image navigation requires knowledge of the spacecraft's position relative to Venus and the pointing direction of the OCPP telescope, which is determined by the telescope's look angle, the spacecraft attitude, and the angular position of the spacecraft in its spin motion. Navigation uncertainties are equivalent to a 2-pixel error in position determination, or a ± 3 m s^{-1} error in the velocity determinations. Drift in the spacecraft attitude and spin rate may introduce another ± 2 m s^{-1} uncertainty. An estimate of the error caused by spurious correlations, which result from changes in the size and shape of the cloud features, is obtained by assuming that the positional uncertainty is approximately equal to the size of those cloud features which change radically in 5 hours. This uncertainty is ~200–400 km, or ± 10–20 m s^{-1} in velocity determination. We believe that these two sources of measurement error are random and, thus that the uncertainty in mean wind speeds shown in Figure 16 caused by these measurement errors is certainly <5 m s^{-1} for most latitudes.

We have tried to determine whether the guided blind technique produces any bias in the measured wind speeds by comparing the results presented to displacement measurements obtained by a manual tracking technique. In this method the positions of a cloud feature in two consecutive images are located by an operator using a computer interactive image display system. Identifying the same cloud feature in both images requires subjective judgements by the operator.

However, a manual measurement of cloud position and a cross-correlation measurement of the displacement, in which the search field is chosen manually, give comparable results. An additional source of error in these manual determinations is the uncertainty in feature identification caused by changes in the illumination and scattering geometry during the motion of a feature. Nevertheless, we estimate the errors in individual manual measurements to be about ±20 m s^{-1}. Comparison of the mean wind speeds determined by guided blind and manual tracking shows a difference of at most 5 m s^{-1} in the zonal wind speeds, although this result may still contain some contribution from random errors.

Studies of the measurement errors are continuing, but we believe that the possible systematic errors in the mean wind speeds shown in Figure 16 are only ~5 m s^{-1}. The poleward direction and the hemispheric asymmetry in the mean meridional wind speed are present in both the manual and the guided blind measurements, however, so that measurement errors, whether random or systematic, do not account for this result.

Acknowledgments. We acknowledge the support of the Pioneer Project staff at Ames Research Center. We thank J. Mendoza for all the photographic processing of the images, W. A. Lane for the computer image processing, and M. Glucksberg and G. Wong for aid in image processing. We are also grateful to N. Habra and E. Goodstadt for vital improvements in the image display system and to C. Grund for the measurement of the cloud-tracked winds. A.D.D. and S.S.L. are supported by NASA/National Research Council resident research associateships.

REFERENCES

Agee, E. M., T. S. Chen, and K. E. Dowell, A review of mesoscale cellular convection, *Bull. Amer. Meteorol. Soc., 54,* 1004–1012, 1973.

Anderson, J. L., M. J. S. Belton, G. E. Danielson, N. Evans, and J. M. Soha, Venus in motion, *Astrophys. J. Suppl. Ser., 36,* 275–284, 1978.

Baines, P. G., The stability of planetary waves on a sphere, *J. Fluid Mech., 73,* 193–213, 1976.

Beebe, R. F., Ultraviolet clouds on Venus: An observational bias, *Icarus, 17,* 602–607, 1972.

Belton, M. J. S., G. R. Smith, D. A. Elliott, K. Klaasen, and G. E. Danielson, Space-time relationships in the UV markings on Venus, *J. Atmos. Sci., 33,* 1383–1393, 1976*a*.

Belton, M. J. S., G. R. Smith, G. Schubert, and A. D. Del Genio, Cloud patterns, waves and convection in the Venus atmosphere, *J. Atmos. Sci., 33,* 1394–1417, 1976*b*.

Blackman, R. B., and J. W. Tukey, *The Measurement of Power Spectra,* 190 pp., Dover, New York, 1958.

Boyer, C., and H. Camichel, Observation photographique de la planète Vénus, *Ann. Astrophys., 24,* 531–535, 1961.

Coffeen, D. L., and J. E. Hansen, Polarization studies of planetary atmospheres, in *Planets, Stars and Nebulae Studied With Photopolarimetry,* edited by T. Gehrels, pp. 518–581, University of Arizona Press, Tucson, 1974.

Colin, L., The Pioneer Venus program, *J. Geophys. Res.,* this issue.

Colin, L., and D. M. Hunten, Pioneer Venus experiment descriptions, *Space Sci. Rev., 20,* 451–525, 1977.

Dollfus, A., Venus: Evolution of the upper atmospheric clouds, *J. Atmos. Sci., 32,* 1060–1070, 1975.

Gierasch, P. J., Meridional circulation and the maintenance of the Venus atmospheric rotation, *J. Atmos. Sci., 32,* 1038–1044, 1975.

Holloway, J. L., Smoothing and filtering of time series and space fields, *Advan. Geophys., 4,* 351–389, 1958.

Julian, P. R., W. M. Washington, L. Hembree, and C. Ridley, On the spectral distribution of large-scale atmospheric kinetic energy, *J. Atmos. Sci., 27,* 376–387, 1970.

Kalnay-Rivas, E., Further numerical calculations of the circulation of the atmosphere of Venus, *J. Atmos. Sci., 32,* 1017–1024, 1975.

Kawabata, K., D. L. Coffeen, J. E. Hansen, W. A. Lane, M. Sato, and L. D. Travis, Cloud and haze properties from Pioneer Venus polarimetry, *J. Geophys. Res.,* this issue.

Knollenberg, R., and D. M. Hunten, The microphysics of the clouds of Venus: Results of the Pioneer Venus particle size spectrometer experiment, *J. Geophys. Res.,* this issue.

Knollenberg, R., L. Travis, M. Tomasko, P. Smith, B. Ragent, D. McCleese, J. Martonchik, and R. Beer, The clouds of Venus, *J. Geophys. Res.,* this issue.

Lacis, A. A., Cloud structure and heating rates in the atmosphere of Venus, *J. Atmos. Sci., 32,* 1107–1124, 1975.

Limaye, S. S., and V. E. Suomi, A normalized view of Venus, *J. Atmos. Sci., 34,* 205–215, 1977.

Limaye, S. S., and V. E. Suomi, Cloud motions on Venus: Global structure and organization, *J. Atmos. Sci.,* in press, 1980.

Murray, B. C., M. J. S. Belton, G. E. Danielson, M. E. Davies, D. Gault, B. Hapke, B. O'Leary, R. G. Strom, V. Suomi, and N. Trask, Venus: Atmospheric motion and structure from Mariner 10 pictures, *Science, 183,* 1307–1315, 1974.

O'Leary, B., Venus: Vertical structure of stratospheric hazes from Mariner 10 pictures, *J. Atmos. Sci., 32,* 1091–1100, 1975.

Ross, F., Photographs of Venus, *Astrophys. J., 68,* 57–92, 1928.

Rossow, W. B., The clouds of Venus, II, An investigation of the influence of coagulation on the observed droplet size distribution, *J. Atmos. Sci., 34,* 417–431, 1977.

Rossow, W. B., Cloud microphysics: Analysis of the clouds of Earth, Venus, Mars, and Jupiter, *Icarus, 36,* 1–50, 1978.

Rossow, W. B., and G. P. Williams, Large-scale motion in the Venus stratosphere, *J. Atmos. Sci., 36,* 377–389, 1979.

Russell, E., L. Watts, S. Pellicori, and D. Coffeen, Orbiter cloud photopolarimeter for the Pioneer Venus mission, *Proc. Soc. Photo Opt. Instrum. Eng., 112,* 28–44, 1977.

Scott, A. H., and E. J. Reese, Venus: Atmospheric rotation, *Icarus, 17,* 589–601, 1972.

Seiff, A., D. B. Kirk, R. E. Young, J. T. Findlay, G. M. Kelly, and S. C. Sommer, Thermal structure, thermal constraints, and dynamical observations in the atmosphere of Venus—Results of in situ measurements from the four Pioneer Venus probes, *J. Geophys. Res.,* this issue.

Stone, P. H., The dynamics of the atmosphere of Venus, *J. Atmos. Sci., 32,* 1005–1016, 1975.

Suomi, V., Cloud motions on Venus, in *The Atmosphere of Venus,* edited by J. E. Hansen, pp. 42–58, Goddard Institute for Space Studies, New York, 1974.

Tomasko, M., P. H. Smith, V. E. Suomi, L. A. Sromovsky, H. E. Revercomb, F. W. Taylor, A. Seiff, R. W. Boese, J. B. Pollack, A. P. Ingersoll, G. Schubert, and C. C. Covey, Thermal balance of Venus in light of the Pioneer Venus mission, *J. Geophys. Res.,* this issue.

Travis, L. D., Nature of the atmospheric dynamics on Venus from power spectrum analysis of Mariner 10 images, *J. Atmos. Sci., 35,* 1584–1595, 1978.

Travis, L. D., Imaging and polarimetry with the Pioneer Venus orbiter cloud photopolarimeter, *Proc. Soc. Photo Opt. Instrum. Eng., 183,* 299–304, 1979.

Travis, L. D., D. L. Coffeen, J. E. Hansen, K. Kawabata, A. A. Lacis, W. A. Lane, S. S. Limaye, and P. H. Stone, Orbiter cloud photopolarimeter investigation, *Science, 203,* 781–785, 1979*a*.

Travis, L. D., D. L. Coffeen, A. D. Del Genio, J. E. Hansen, K. Kawabata, A. A. Lacis, W. A. Lane, S. S. Limaye, W. B. Rossow, and P. H. Stone, Cloud images from the Pioneer Venus orbiter, *Science, 205,* 74–76, 1979*b*.

Wright, W. H., Photographs of Venus made by infrared and by violet light, *Publ. Astron. Soc. Pac., 39,* 220–221, 1927.

(Received December 13, 1979;
revised May 1, 1980;
accepted May 2, 1980.)